Influence of intraseasonal eastern boundary circulation variability on hydrography and biogeochemistry off Peru

Jan Lüdke[1], Marcus Dengler[1], Stefan Sommer[1], David Clemens[1], Sören Thomsen[2], Gerd Krahmann[1], Andrew W. Dale[1], Eric P. Achterberg[1,3], Martin Visbeck[1,3]

[1]GEOMAR Helmholtz Centre for Ocean Research Kiel, Düsternbrooker Weg 20, D-24105 Kiel, Germany

[2]LOCEAN-IPSL, IRD/CNRS/Sorbonnes Universites (UPMC)/MNHN, UMR 7159, Paris, France

[3]Kiel University, Kiel, Germany

Correspondence to: Jan Lüdke (jluedke@geomar.de)

Abstract.

The intraseasonal evolution of physical and biogeochemical properties during a coastal trapped wave event off central Peru is analysed using data from an extensive shipboard observational programme conducted between April and June 2017, and remote sensing data. The poleward velocities in the Peru Chile Undercurrent were highly variable and strongly intensified to above 0.5 m s^{-1} between mid and end of May. This intensification was likely caused by a first baroclinic mode downwelling coastal trapped wave, excited by a westerly wind anomaly at the equator at about 95° W. Local winds along the South American coast did not impact the wave. Although there is general agreement between the observed cross-shore-depth velocity structure of the coastal trapped wave and the velocity structure of first vertical mode solution of a linear wave model, there are differences in the details of the two flow distributions. The enhanced poleward flow increased water mass advection from the equatorial current system to the study site. The resulting shorter alongshore transit times between the equator and the coast off central Peru led to a strong increase in nitrate concentrations, less anoxic water, likely less fixed nitrogen loss to N$_2$, and a decrease of the nitrogen deficit compared to the situation before the poleward flow intensification. This study highlights the role of changes in the alongshore advection due to coastal trapped waves for the nutrient budget and the cumulative strength of N-cycling in the Peruvian oxygen minimum zone. Enhanced availability of nitrate may impact a range of pelagic and benthic elemental cycles, as it represents a major electron acceptor for organic carbon degradation during denitrification and is involved in sulfide oxidation in sediments.

1 Introduction

The Peruvian Upwelling System (PUS) is one of the most productive regions in the world's ocean with economically important fish catches (e.g. Carr, 2002; Chavez et al., 2008). Located in the Eastern Tropical South Pacific (ETSP), the high surface productivity of the PUS is most pronounced within a 100 km wide stretch along the Peruvian coast between 4° and 16° S (Pennington et al., 2006). Equatorward winds favour upwelling throughout the year (Bakun and Nelson, 1991; Strub et al., 1998) and enable a supply of nutrients from subsurface waters and benthic boundary layer to the euphotic zone, stimulating high primary productivity (Pennington et al., 2006). Below the surface layer, low oxygen waters supplied to the PUS and enhanced local oxygen consumption due to remineralization of exported organic matter lead to the development of a pronounced Oxygen Minimum Zone (OMZ). The core of the OMZ with upper and lower bounds at about 30 – 200 m and 400 – 500 m depth, respectively, is considered to be functionally anoxic (e.g. Ulloa et al., 2012, Thomsen et al. 2016).

The eastern boundary circulation in the PUS is dominated by the poleward Peru-Chile Undercurrent (PCUC) occupying the upper continental slope and shelf at depths from 50 to 200 m (Fig. 1, e.g. Gunter, 1936; Chaigneau et al., 2013). It carries low-

oxygen and high-nutrient Equatorial Subsurface Waters (ESSW), which constitutes the main source of the upwelled waters (Silva et al., 2009; Albert et al., 2010). Mean poleward velocities associated with the PCUC are between 0.05 and 0.15 ms^{-1} (Chaigneau et al., 2013). The origin of its source waters is still under debate. Chaigneau et al., (2013) traced its source waters

40   to the Equatorial Undercurrent supplying the PCUC via the Ecuador-Peru Coastal Current, that flows poleward along the coast between the equator and 5° S. In contrast, a regional model analysis by Montes et al. (2010) suggests that the source waters of the PCUC originate predominately from the eastward Southern Subsurface Countercurrents, flowing south of the equator (Fig. 1). Above the PCUC, upwelling dynamics imply the existence of an equatorward geostrophic surface jet, known as the Peru Coastal Current (e.g. Hill et al., 1998; Kämpf and Chapman, 2016). Additional features of the eastern boundary circulation are

45   the Peru-Chile Current flowing equatorward offshore of the PCUC, and the Chile-Peru Deep Coastal Current flowing equatorward below the PCUC (Fig. 1, Strub et al., 1998; Chaigneau et al., 2013).

The PUS exhibits variability on a wide range of timescales, including intraseasonal (e.g. Gutiérrez et al., 2008; Illig et al., 2018a, 2018b), seasonal (e.g. Pizarro et al., 2002), and interannual to decadal (e.g. Graco et al., 2017). Intraseasonal variability of oxygen and nutrient concentrations along the Peruvian margin are known to strongly impact pelagic and benthic ecosystems

50   within the OMZ and the upwelling region above (e.g. Gutiérrez et al., 2008; Echevin et al., 2014; Graco et al., 2017).

A key factor thought to be responsible for the intraseasonal variability of oxygen and nutrient concentrations is the variability of the eastern boundary circulation, forced locally by changes of the wind system above the PUS or forced remotely by variability of the wind system at the equator. Strengthening (weakening) of the local alongshore winds causes intensified (reduced) Ekman divergence close to the coast that accelerates (decelerates) the coastal surface jet (e.g. Philander and Yoon,

55   1982; Fennel et al., 2012). Coastal Trapped Waves (CTWs) are excited and propagate poleward to set up an alongshore pressure gradient balancing an accelerating (decelerating) alongshore flow (Yoon and Philander, 1982). Due to differences in vertical structure of the surface jet and the excited CTWs, the poleward flowing PCUC accelerates (decelerates). Furthermore, variability of local wind stress curl forces variability of the poleward undercurrent by affecting the magnitude of Sverdrup transport in the eastern boundary current regime (e.g. McCreary and Chao, 1985; Klenz et al., 2018). Variability of local wind

60   stress curl forces also variability of time scales from intra-seasonal to seasonal (e.g. Marchesiello et al., 2003, Junker et al., 2015, Klenz et al., 2018).

Alternatively, variability of zonal winds in the equatorial Pacific forces equatorial Kelvin waves that propagate eastward. Upon reaching the continental margin, part of their incoming energy is transmitted poleward along the southwestern coast of South America as CTWs (e.g. Moore and Philander, 1977; Enfield et al., 1987). Early measurement programs off Peru investigating

65   intraseasonal alongshore current variability showed coherent CTW signals with periods of 5-50 days propagating poleward between 5° S and 15° S (Brink et al., 1980, 1983; Romea and Smith, 1983). Tide gauge data and a lack of correlated local winds suggested that the CTWs were predominately of equatorial origin. Similarly, intraseasonal CTW variability (50-day period) in the PCUC off Chile with velocity amplitudes of up to 0.7 m s^{-1} were shown to have originated from wind variability in the central equatorial Pacific (Shaffer et al., 1997). Modelling efforts confirm that equatorially-forced intraseasonal CTWs

70   propagate along the eastern South American coast to as far as 30° S (Hormazabal et al., 2002; Illig et al., 2018b).

Poleward propagating CTWs produce vertical displacements of the pycnocline of the order of tens of meters and sea level changes of a few centimeters (Leth and Middelton, 2006; Belmadani et al., 2012). They also modulate the alongshore circulation, that is, CTWs that have a positive sea level anomaly and a downward displacement of the thermocline (downwelling waves) exhibit poleward flow while CTW that have a negative sea level anomaly (upwelling waves) exhibit

75   equatorward flow (e.g. Echevin et al., 2014). The combined effect alters the horizontal and vertical supply of nutrients in the PUS. Modelling and satellite observations suggest that subsurface nutrient and chlorophyll intraseasonal variability in the PUS are mainly forced by remotely forced CTWs (Echevin et al., 2014). The simulations indicate that the shoaling and deepening of the nutricline, as well as the horizontal currents associated with the CTW, induce a nutrient flux in and out of the euphotic layer, which impacts primary production. On the other hand, intraseasonal sea surface temperature (SST) variability is

suggested to be mainly driven by local winds and heat fluxes with CTWs playing only a minor role (Dewitte et al., 2011; Illig et al., 2014). Variability of CTWs can affect hence nutrient concentrations and bottom water oxygen levels (Graco et al., 2017) on intra-seasonal but also inter-annual timescales. The benthic biota reacts strongly to periods of oxygenation or deoxygenation, which are caused by CTWs, and the dominant benthic community changes from macro-invertebrates to bacterial mats (*Thioploca/Beggiatoa*) after prolonged low-oxygen conditions (Gutiérrez et al., 2008) and benthic sulfide emissions and toxic sulfide plumes in the water column can occur (Schunck et al., 2013; Dale et al., 2016).

Here, we use an extensive multi-parameter data set from a multi-cruise observational program to analyse the impact of a strongly elevated and individual propagating CTW on the circulation, hydrography and nutrient concentrations in the PUS. By visiting sampling stations several times over a period of more than two months, we measured the variability of the circulation and hydrographic and biogeochemical conditions almost continuously and can distinguish the intraseasonal variability from processes taking place on shorter time scales.

The conditions off Peru in early 2017 were further affected by anomalously warm temperatures in the upper ocean during March associated with a coastal El Niño event (e.g. Garreaud, 2018; Echevin et al., 2018). Our observations cover the declining phase of the coastal El Niño event in April and May when SST anomalies were decreasing.

2 Data

2.1 Ship data

Within the framework of the Collaborative Research Center 754 "Climate-Biogeochemistry Interactions in the Tropical Ocean", we carried out a combined physical and biogeochemical sampling program in the ETSP from April to June 2017 during several legs on R/V Meteor (Tab. 1). A regional focus during the four individual cruises of the sampling program was a transect starting at shallow waters off Callao (Peru) at about 12° S running offshore perpendicular to the coastline and ends at water depths greater than 5000 m and more than 100 km offshore (Fig. 1). During the first R/V Meteor cruise M135, the 12° S section was studied towards the end of the cruise (April 7 – 8). The two subsequent cruises M136 and M137 focused on benthic and pelagic work off Peru between 11° and 14° S (Dengler and Sommer, 2019; Sommer et al., 2019). Benthic lander measurements required the vessel to remain close to the section between April 18 and May 29, 2017, when repeated hydrographic and velocity measurements along the section were collected. The section was again sampled during the final cruise M138 (June 24). In this study, we analyse shipboard velocity data, hydrographic profiles as well as oxygen and nutrient concentration measurements from the repeated measurements along 12° S.

2.1.1 Shipboard velocity observations

Upper ocean velocities were recorded continuously using two vessel-mounted Ocean Surveyor Acoustic Doppler Current Profiler systems (vmADCP) installed on R/V Meteor. One vmADCP was operated at a frequency of 75 kHz (OS75) and its system configuration during the cruises varied only in depth bin settings. Depth bins of 4, 8 or 16 m were chosen depending on strength of the backscatter signal and the focus of the investigation, allowing a maximum range of 750 m. The second vmADCP operated at 38 kHz (OS38) and recorded depth bins of 32 m while sampling an increased depth range (30 – 1000 m). During post-processing, vmADCP velocities were corrected using a mean amplitude and misalignment angle determined from water-track calibration (e.g. Fischer et al., 2003). Misalignment angles derived from individual ship accelerations and turns followed a Gaussian distribution having a standard deviation of less than 0.65° for the OS75 and less than 0.75° for the OS38 (Sommer et al., 2019). A temporal trend was not detectable. The uncertainty of the misalignment angle calibration can be determined from its standard deviation divided by the square root of the number of independent estimates (e.g. Fischer et al., 2003). For our data, more than 100 independent estimates were available for each cruise, resulting in an angle uncertainty

of less than 0.1° and an associated velocity bias of less than 1 cm s^{-1} for underway data. Fischer et al. (2003) suggested an accuracy of 3 cm s^{-1} for hourly underway data recorded during calm conditions in the tropics.

2.1.2 Hydrographic observations

Along the 12° S section, a total of 151 hydrographic profiles were collected during cruises M136 and M137 with a lowered SeaBird SBE 9-plus conductivity-temperature-depth (CTD) system using double sensor packages for temperature, conductivity and oxygen. The CTD was attached to a General Oceanics rosette with 24 Niskin bottles of 10 l to collect water samples. For the calibration of the conductivity sensor, water samples were analysed with a Guildline Autosal Salinometer model 8400 B. Correction coefficients for the CTD's conductivity sensors were derived using a multiparameter fit of the Autosal conductivities against the uncalibrated CTD sensor measurements.

CTD oxygen sensors were calibrated against oxygen concentrations determined from bottle water samples using Winkler titration (Winkler, 1888; Grasshoff et al., 1983). Processing and calibration followed the GO-SHIP recommendations (Hood et al., 2010). Previous studies using Switchable Trace amount OXygen (STOX) sensors have shown that the core of the Peruvian OMZ is functionally anoxic (Revsbech et al., 2009; Thomsen et al., 2016). Unfortunately, the Winkler titration method fails to accurately determine very low oxygen concentrations from bottle water samples. To assure anoxic conditions in the OMZ core, a mean oxygen concentration offset of 2.26 µmol l^{-1} was subtracted from low oxygen values. Calibration of the salinity and oxygen sensors was performed separately for each cruise, except for M136 where the mean of the calibration of the preceding and succeeding cruises M135 and M137 was used (M136 lacked deep-water samples required for calibration purposes). The final post-cruise calibration of the data resulted in an accuracy for temperature, salinity, and oxygen of 0.002° C, 0.002 g kg^{-1} and 1.5 µmol kg^{-1}, respectively.

2.1.3 Nutrient measurements

Water samples collected during the upcast of the CTD rosette were used to determine nutrient concentrations. Concentrations of nitrate, nitrite and phosphate were measured using a QuAAtro autoanalyzer (Seal Analytical) with a precision of 0.1 µmol l^{-1}, 0.1 µmol l^{-1}, and 0.2 µmol l^{-1}, respectively (Sommer et al., 2019). Ammonium concentrations were measured using a fluorimetric method (Holmes et al., 1999).

In addition, concentrations of nitrate were measured using a Satlantic Deep Submersible Ultraviolet Nitrate Analyzer (SUNA) mounted on the CTD rosette (Hauschildt et al., 2020). SUNA measurements are based on the absorbance spectra of ultraviolet light (Sakamoto et al., 2009). Data post-processing followed Karstensen et al. (2017) and Thomsen et al. (2019). In a final step, the SUNA nitrate concentrations were calibrated against the nitrate concentrations from the CTD water samples using a linear fit.

2.2 Additional data

Additional regional data sets from satellite observations were used to supplement our analysis of ship-board observations. Sea Level Anomaly (SLA) data based on satellite altimeter measurements were provided by the E.U. Copernicus Marine Environmental Monitoring Service (product: SEALEVEL_GLO_PHY_L4_REP_OBSERVATIONS_008_047). This is a level 4 dataset derived by merging all available satellite altimetry data into one gridded product. Reprocessed data from January 1, 1993 to January 1, 2018 with the release days January 15, 2018 (data before May 15, 2017) and May 16, 2018 was accessed. Additionally, sea surface temperature from the NOAA Extended Reconstructed Sea Surface Temperature, Version 5 (ERSSTv5) dataset (Huang et al., 2017a) was analyzed. This dataset provides monthly values of SST on a 2°x2° grid based on in-situ temperature observations from several sources (Huang et al., 2017b). Finally, wind stress data from the ASCAT product of satellite scatterometer winds (Bentamy and Fillon, 2012) was analyzed. This product provides daily global winds and wind stress data with a resolution of 0.25°.

3 Methods

3.1 Analysis of velocity observations

The continuous velocity recording was split into segments when the ship was moving in on- or offshore directions only. The velocities were rotated to derive the alongshore component and then a mean velocity section was calculated for each segment of the cruise in 2 km bins according to offshore distance. Periods where the ship was moving slower than 1 kn were excluded. To derive the sections of alongshore velocity over longer time periods, the data from several of these segments were averaged. The presented sections were smoothed using a 2-D Gaussian weights.

3.2 Analysis of hydrographic and biogeochemical data

The analysis of hydrographic data was based on the TEOS10 definitions (IOC et al., 2010). Conservative temperature, absolute salinity, density and potential density anomalies were calculated with the Matlab Gibbs Seawater Toolbox (McDougall and Barker, 2011; Version 3.05). Nutrient concentrations were transformed to $\mu mol\ kg^{-1}$ to remove the effect of compressibility on vertical gradients. In the following we mean conservative temperature when we refer to temperature and absolute salinity when we refer to salinity.

3.2.1 Nitrogen deficit

In suboxic environments, microbially mediated processes such as denitrification and anaerobic ammonium oxidation (anammox) transform biologically available reactive nitrogen (nitrate, nitrite, and ammonium) via intermediate steps into dinitrogen (N_2), which cannot be used by most organisms (dinitrogen, N_2). These processes lead to a loss of reactive nitrogen relative to other nutrients such as phosphate (PO_4^{3-}). The global distribution of nitrate, phosphate and dissolved inorganic carbon (DIC) display a strong covariation, with a slope of N:P of about 16:1 reflecting the mean stoichiometry of organic matter synthesis and degradation. In order to analyze the impact of nitrogen loss and N_2-fixation on the NO_3^- distribution it is convenient to remove the photosynthesis/remineralization trend and only focus on deviations, N*, from this trend. The concept of N* has been introduced (Gruber & Sarmiento 1997, 2002). Here, the formulation of Chang et al. (2010) was applied to investigate the nitrogen deficit, N_{def}, $\mu mol\ kg^{-1}$. It is based on the deviation from the ratio between nitrogen species and phosphate outside of the eastern tropical south Pacific OMZ. The nitrogen deficit is calculated as:

$$N_{def} = 15.8\ (PO_4^{3-} - 0.3) - (NO_3^- + NO_2^- + NH_4^+) \tag{1}$$

Where PO_4^{3-}, NO_3^-, NO_2^-, and NH_4^+ are the concentrations of phosphate, nitrate, nitrite and ammonium, respectively. With this definition, positive values of N_{def} quantify an N-loss that has occurred within a certain water mass while it remained in the Peruvian OMZ.

3.2.2 Section averaging

Smoothed hydrographic and biogeochemical properties along the 12° S section were calculated by interpolating the data vertically onto common potential density surfaces. Averaging in density space removes the effect of signal smearing due to vertical displacement caused by internal waves. The profiles were then averaged in bins of 2 km according to distance from the coastline and then smoothed using 2-D Gaussian weights. In a final step, the averaged and smoothed sections were vertically transformed back into depth space using the smoothed depth – density relation.

3.3 Sea level anomaly and wind data

The local SLA along the 12° S section was calculated by first averaging all daily gridded SLA data between 12° and 12.5° S over the time periods used for the velocity sections and interpolating them onto the section according to the distance to the coast. Grid points closer than 30 km to the coast were excluded. Then the mean SLA along the section was subtracted to focus on the cross-shore gradient. In addition, intraseasonal variability along the equator and coastline was analysed by subtracting the mean SLA over the 25-year time series before bandpass filtering SLA using a 4th order Butterworth filter for a time window between 20 and 90 days. To follow intraseasonal SLA variability due to propagating waves along the equator and subsequently along the western South American coast, we used bandpass filtered SLA data averaged between 0.25° S and 0.25° N from the equator and two-grid-points averages from near the coast.

For investigating wind forcing of Kelvin waves at the equator, SLA and zonal wind anomaly were averaged to five-day means over 10° of longitude. Additionally, wind anomaly was averaged between 5° N and 5° S while SLA was averaged between 2° N and 2° S.

3.4 Theoretical coastal trapped wave structure

To interpret the observed flow variability along the Peruvian coast in terms of CTWs, the cross-shore-depth structure of CTWs was determined by considering the linear, hydrostatic, inviscid, and Boussinesq approximated equations of motion on an f-plane using local bathymetry and stratification (Brink, 1982; 1989; Illig et al., 2018a). For alongshore scales larger than cross-shore scales and horizontally uniform stratification, cross-shore-vertical mode structures (eigenfunctions) and corresponding phase velocities (eigenvalues) solutions were obtained from the simplified set of equations by using a resonance iteration approach (Brink, 1982; Brink and Chapman, 1987). Here, we obtained the eigenfunctions and eigenvalues for the first three modes by applying a modified version of the Brink and Chapman (1987) Coastal-Trapped Wave programs as published by Brink (2018).

Local bathymetry and stratification are required as input to Brink's (2018) set of Matlab mfiles. The cross-shore distribution of bathymetry was taken from the multi-beam echo sounder data collected during the cruises along 12° S. Echo sounder data was averaged in 5 km bins which resulted in a monotonic increase of water depth in an offshore direction. The maximum water depth used for the wave solutions was 5000 m. From two offshore CTD profiles (M136 #60 and M137 #92) exceeding 3000 m depth, a stratification profile was calculated first for each profile using 20 data points with 1 dbar spacing and then a mean profile was calculated from both casts in 5 m intervals.

4 Results

4.1 Variability of the boundary circulation

The direct velocity observations from the multi-cruise program allowed a detailed assessment of the variability of the eastern boundary alongshore velocity structure at 12° S for a period of more than eleven weeks (Fig. 2). During the observational period from early April to June 24 (2017), we captured an event of strongly increased poleward flow that started in early May and lasted for about 35 days.

The time series started with two days of sampling in April 7 to 8. During this period, a distinct poleward flowing PCUC was present that extended 80 km offshore (Fig. 2a) and had maximum velocities of more than 0.3 m s^{-1} on the continental shelf. Satellite altimetry indicated an increasing SLA towards the coast (Fig, 2a upper subpanel). Between April 18 and May 26, and except for a short break from May 4 to 6, the 12° S section was continuously surveyed. In mid-April, a poleward flow was present only on the shelf (Fig. 2b). However, from the end of April to mid-May, the PCUC considerably strengthened reaching maximum core velocities of about 0.5 m s^{-1} between 50 and 100 m depth 50 km offshore (Fig. 2c, d and e). Furthermore, the PCUC poleward flow extended to more than 80 km offshore and occupied the water column above 400 m depth. The SLA

increased towards the coast (by 2 cm over 40 km) implying that a poleward geostrophic velocity anomaly was present at the sea surface as well. Towards the end of May, poleward flow in the PCUC did not increase further, but remained at a similar level as during mid-May (Fig 2f). In contrast, velocity data from a final section occupation 3 weeks later in June 24 shows evidence that the PCUC had weakened drastically (Fig. 2g), exhibiting a comparable velocity distribution as for the period April 18-25 (Fig. 2b). Assuming similar time scales for its deceleration as for its acceleration, the period of intensified PCUC flow was between 30 to 40 days. The intensified PCUC flow strongly exceeded the climatological PCUC flow reported from this region. Mean alongshore flow at 12° S determined from vmADCP data sampled during 22 cruises showed maximum PCUC core velocities of 0.1 – 0.15 m s^{-1} (Chaigneau et al., 2013), similar to the situation observed during April 18-25 and June 24 (Fig. 2b and g).

In April, the velocity sections indicated an equatorward flow offshore and below the PCUC (Fig. 2). The Peru Coastal Current and the Chile-Peru Deep Coastal Current are thought to be located at these depths and offshore ranges (e.g. Penven et al., 2005; Chaigneau et al., 2013). In late April, the equatorward flow increased in strength and extended to shallower depths (Fig. 2b and c). However, during the period of strong poleward flow in May, the equatorward flow decreased and was present only below 400 m depth close to the offshore end of the section (Fig. 2e and f). On June 24, a weak equatorward flow was present below 200 m at most parts of the section but never reached velocities of 0.1 m s^{-1}. We found no indication of equatorward flow above or inshore of the PCUC, where the equatorward surface jet is expected to be situated. The lack of this surface flow in observations was also noted by Chaigneau et al. (2013).

To compare the alongshore circulation with hydrographic and biogeochemical sampling, the data were averaged into two periods: The initial phase of weak poleward flow (Fig. 3a) covering the period from April 18 – May 3, and a period of enhanced poleward flow 12 – 26 May (Fig. 3b). The increase in poleward velocities was especially strong between 40 and 60 km offshore where velocities increased from about zero to 0.4 m s^{-1} (Fig. 3c). The core of velocity increase extended deeper than the intensified PCUC and was more detached from the coast.

4.2 Potential causes of circulation variability

4.2.1 Role of local wind stress

Changes in the local wind stress curl are a potential local forcing mechanism of an intensified PCUC flow. An increase in the magnitude of near-coastal negative wind stress curl leads to an increased poleward flow along the eastern boundary through Sverdrup dynamics (e.g., Marchesiello et al., 2003). The adjustment of the circulation to changes in the wind stress curl at the eastern boundary is rather fast and occurs within a few days (Klenz et al., 2018). Wind stress curl along the Peruvian continental margin between 10° S and 14° S was negative throughout the observational period (Fig. 4), continuously forcing poleward flow. However, during the period of PCUC acceleration between end of April and mid-May, the magnitude of negative wind stress curl decreased (Fig. 4c, d, e, f). It can thus be ruled out that local wind stress curl forcing is responsible for the observed intensified PCUC. Nevertheless, elevated negative wind stress curl was observed from May 18 – 22, which may have contributed to maintain a strong PCUC in late-May.

Variability of near-coastal alongshore wind stress excites CTWs that propagate poleward (e.g. Yoon and Philander, 1982) and thereby enhances or decreases poleward flow within the depth range of the PCUC. From mid-April until May 2017, alongshore wind stress between 6° S and 15° S was variable (Fig. 5). While moderate wind stress (0.03 – 0.06 N m^{-2}) prevailed from mid-April to May 3, it was weak during the first two weeks of May (Fig. 5d, e, g). On May 15, the wind stress increased and remained elevated for a period of about 5 days. This wind variability cannot explain the observed changes in poleward transport. The poleward transport increased from late April to its maximum mid-May, whereas the alongshore wind stress during this period decreased in the first week and then increased seven days later.

4.2.2 Equatorial winds and wave response

According to equatorial linear wave theory a weakening of the trade winds at the equator by e.g. westerly wind events, generates eastward propagating equatorial Kelvin wave. Once the equatorial Kelvin wave interacts with the eastern boundary parts of its energy are transmitted to a CTW (Enfield et al., 1987). Indeed, several westerly wind anomalies occurred in the central and eastern equatorial Pacific during the first 6 months of 2017 (Fig. 6). A particularly elevated westerly wind anomaly occurred between the international date line and 120° W during the first two weeks of April (Fig. 6a). In response, a positive SLA propagating along the equator appeared to the east of the wind event between about 100° W and 80° W (Fig. 6b dash line, Fig. 7) and arrived at the eastern boundary at the beginning of May.

Bandpass-filtered SLA data from the equator and from near the continental slope (section 3.3) along the South American continent (Fig. 7) indicate that the positive SLA arriving at the eastern boundary continued southward along the eastern boundary to about 14° S. Along the equator, the propagation speed of the SLA was about 2.7 m s^{-1} (dashed line in the left panel of Fig. 7), which agrees with the phase speed of a first vertical mode equatorial Kelvin waves (e.g. Yu and McPhaden, 1999). The speed of propagation of the SLA signal along the eastern boundary was somewhat enhanced and around 3 m s^{-1}. A positive SLA signal was associated with a negative (downward) displacement of the thermocline, eastward upper-ocean velocities at the equator and poleward upper-ocean velocities at the continental slope. This agrees well with the SLA signal and the increased poleward PCUC velocities at 12° S and suggests the existence of a downwelling CTW during May 2017. Additionally, the speed of propagation at the equator indicates a first baroclinic mode Kelvin wave arriving at the eastern boundary.

4.2.3 Modal structure of the intensified flow

To further investigate the nature of the boundary flow intensification, the cross-shore-depth structure of alongshore velocity was determined for the first three CTW modes at 12° S (Fig. 8, see section 3.4 for a description of the model used). Due to a steep continental slope at 12° S, the velocity structure of the different CTW solutions varied predominately in the vertical axis with poles of opposing velocity located above each other (Fig. 8). Flow reversal for each individual mode away from the boundary occurs at shallower depth compared to inshore regions. Higher modes exhibit an upper pole of enhanced velocity located at shallower depth compared to lower modes.

For comparison, Fig. 8e shows the difference of full-depth low-frequency vmADCP alongshore velocities between May 12 to 26 and April 18 to May 3. Apart from the increased poleward velocity in the upper 500 m, the alongshore velocity difference resolved by the OS38 was weakly poleward throughout the upper 1000 m of the water column (Fig. 8e). Comparing the baroclinic structure of the observations to the baroclinic structure of the different CTW modes, the missing flow reversal in the upper 1000 m shows that the observed change in alongshore velocity is best described by a first mode CTW. This mode features poleward flow anomalies throughout the upper 1500 m (Fig. 8b) which agrees with the distribution of the velocity differences between the two time periods throughout most of the upper 1000 m (Fig. 8e). The maximum increase of poleward flow, on the other hand, was restricted to a depth range similar to the upper poleward velocity core of a second mode CTW. Additional support for the presence of first mode CTW originates from a comparison of the phase speeds. At 12° S, the local phase speeds of the model CTW modes (Fig. 8) were higher than those for equatorial Kelvin waves. In particular, the phase speed of the first mode CTW was 3.1 ms^{-1}, which agrees very well with the phase propagation of the SLA signal discussed in section 4.2.2.

4.3 Response of hydrographic conditions to the PCUC intensification

In the following, we analyse the changes in hydrographic conditions co-occurring with the increase of the alongshore flow. Lower near-surface temperatures near the coast compared to offshore (Fig. 1, Fig. 9a, b) indicated active upwelling during the observational program. While the upwelling signal was restricted to the upper 50 m, near-coastal water masses between 50 m

and 300 m were significantly warmer compared to water masses offshore (Fig. 9a). During the intensified PCUC period (Fig. 9 middle panels), the cross-shore temperature gradient intensified, leading to an increased downward displacement of isopycnals and isotherms near the coast (Fig. 9b). There, the associated warming signal between 100 m and 200 m depth was up to 0.5° C. Note that during the PCUC intensified period, near-coastal surface temperatures decreased.

320 Salinity featured a shallow subsurface salinity maximum at about 25 m depth originating offshore and extending over the slope and shelf (Fig. 9d and e). As for temperature, cross-shore salinity gradients were evident between 50 and 300 m depth with higher salinities near the coast which intensified when the PCUC increased. At the same time, salinity at the upper shelf decreased (Fig. 9f).

Distribution of oxygen concentrations were characterized by a sharp oxycline above the anoxic OMZ (Fig. 9g and h). During 325 the weak PCUC period, oxygen concentrations decreased from slightly supersaturated at the surface to anoxia within the upper 100 m of the water column (Fig. 9g). Between 450 and 500 m, oxygen concentrations started to increase again to detectable values (Fig. 9g). When the poleward flow intensified, oxygen levels of waters below about 100 m depth increased (Fig. 9i) and low oxygen waters were found deeper in the water column than previously (Fig. 9h). Part of the increased oxygen levels were due to the downward displacement of the isopycnals (Fig. 9h), particularly in the near-bottom waters above the 330 continental slope. There, oxygen concentrations larger than 2 µmol kg^{-1} were observed at 200 m depth in bottom waters (Fig. 9h), a depth range that is usually occupied by anoxic water masses. Such ventilation events have significant consequences for benthic and pelagic biota and for biogeochemical processes in that depth range, as further discussed below.

In the upper water column above 400m, waters with potential density anomalies larger than 25.9 kg m^{-3} were predominantly Equatorial Subsurface Water (ESSW; Fig. 10). ESSW originates from the equatorial current system. It is characterized by a 335 linear relationship of temperature and salinity in the temperature range 8 – 14 °C and salinity range 34.6 – 35.0 (e.g. Grados et al., 2018). Lower salinity Eastern South Pacific Intermediate Water (temperature range 12 – 14 °C, salinity 34.8), which is also situated in the depth range mentioned above, was only observed in the hydrographic data from two offshore stations (Fig. 10a). The dominance of ESSW was not affected by the increasing poleward velocities (Fig. 10b) and most profiles followed the same temperature and salinity relationship in both phases. In fact, during PCUC intensification, the ESSW was the sole 340 water mass in the upper 400 m within 80 km of the coast (Fig. 10b).

4.4 Response of nutrient biogeochemistry to PCUC intensification

Nutrients are supplied to the upwelling region by poleward transport within the PCUC. In the following, we relate the observed changes in nutrient concentrations to the PCUC variability and to microbially-mediated biogeochemical processes (section 3.2.1). In the anoxic core of the OMZ denitrification represents a prominent process of anaerobic organic matter degradation 345 and a major sink for reactive nitrogen (Kavelage et al., 2013, Gruber 2008). During denitrification, nitrate is stepwise reduced to N_2, with nitrite and nitrous oxide, as important intermediate products. Subsequently, nitrite is either further reduced to N_2 via denitrification or may be used in the microbially driven anaerobic oxidation of NH_4^+ to N_2 known as annamox (Kuypers et al. 2005, Lam et al. 2009), which leads to a loss of reactive nitrogen. The distributions of nitrate (Fig. 11a and b) and nitrite concentrations (Fig. 11d and e) demonstrate the transformation of nitrate to nitrite. In the open ocean nitrate increases with 350 depth in the upper 1000 m, whereas on the Peruvian margin a nitrate minimum in the anoxic core of the OMZ is pronounced at 12° S (Fig. 11a and b), co-occurring with a maximum in nitrite.

During the period of PCUC intensification, nitrate concentrations on the shelf and upper slope increased (Fig. 11a and b). Before the intensification, nitrate concentrations in the upper 300 m of the water column hardly exceeded 25 µmol kg^{-1} and particularly low concentrations were found in bottom waters on the shelf, where a local minimum with less than 15 µmol kg^{-1} 355 is reached (Fig. 11a). As the PCUC intensified, nitrate concentrations between 50 m and 250 m mostly exceeded 25 µmol kg^{-1} (Fig. 11b). Throughout this part of the section, the increase was higher than 2.5 µmol kg^{-1} (Fig. 11c), and in some areas exceeded 5 µmol kg^{-1}.

On the other hand, nitrite concentrations in deeper and bottom waters on the shelf and upper slope were reduced during the intensified PCUC period (Fig. 11d and e). In general, nitrite concentrations in oxygenated waters ($O_2 > 2$ µmol kg^{-1}) were less than 1 µmol kg^{-1}, which is likely due to nitrification. In the anoxic core of the OMZ, the nitrite distribution featured two maxima; one in the upper part of the OMZ between 150 m and 200 m depth and another in the centre of the OMZ at 300 m depth, both having concentrations of up to 5 µmol kg^{-1}. During the PCUC intensification period, the upper boundary of nitrite containing water was displaced downwards (Fig. 11e) following the displacement of anoxic waters (Fig. 9h). This caused a nitrite decrease exceeding 2 µmol kg^{-1} in the deeper and bottom water on the continental slope at about 200 m depth (Fig. 11f).

Ammonium concentrations were generally low or undetectable. Concentrations in excess of 0.4 µmol kg^{-1} occurred only close to the surface on the upper shelf (Fig. 11g and h). It should be noted that in the Peruvian upwelling region, the sediments are a strong source of ammonium (e.g. Sommer et al., 2016). However, despite taking water samples for nutrient analysis very close to the sea floor, elevated ammonium concentrations could not be detected, suggesting a fast removal by annamox of ammonium which was released from the sediments. In case oxygen was present, ammonium could also have been nitrified to nitrate.

Phosphate concentrations did not change considerably during the PCUC intensification period (Fig. 11j and k). Concentrations were low at the surface and increased to 2 µmol kg^{-1} at 50 m depth. Within the upper OMZ, the concentrations were higher offshore than onshore (Fig. 11j and k). When the PCUC intensified, concentrations decreased in approximately the same region in which the nitrate increase occurred (Fig. 11l). A phosphate decrease of up to 0.3 µmol kg^{-1} occurred in bottom waters on the shelf at water depths shallower than 100 m.

The nitrogen deficit (N_{def}, section 3.2.1) was reduced during the period of PCUC intensification (Fig. 11m, n and o). Whilst the PCUC was weak, waters having a nitrogen deficit between 5 µmol kg^{-1} and 15 µmol kg^{-1} were present at depths between 100 m and 400 m. Maximum values were found on the continental shelf and offshore between 100 m and 200 m (Fig. 11m). During the PCUC intensification period, the nitrogen deficit maximum at the continental shelf disappeared and low deficit waters ($N_{def} < 5$ µmol kg^{-1}) occupied the upper 200 m of the water column inshore of 40 km (Fig. 11n). The reduced nitrogen deficit was due increased nitrate concentrations (Fig. 11c) and somewhat reduced phosphate concentrations (Fig. 11l). Furthermore, the region with reduced N_{def} agrees well with the location of maximum poleward flow during the PCUC intensification period (Fig. 3b). This suggests that poleward advection in the intensified PCUC was the main cause for the observed changes in biogeochemical properties.

5 Summary and Discussion

Measurements from an intensive physical and biogeochemical shipboard sampling program off Peru at 12° S carried out between April 7 and June 24 2017 are used to analyse intraseasonal variability of the eastern boundary circulation and associated changes in hydrography and nutrient distributions. The Our most prominent finding is an intensification of poleward flow within the depth range occupied by the PCUC that started early May 2017 and lasted for about 35 days. During this period, poleward velocities occupied the whole water column above 1000 m depth and extended to more than 80 km offshore. Maximum velocities in the PCUC core between 50 m and 100 m depth were above 0.5 m s^{-1}, about 5 times larger than the respective climatological PCUC velocities (Chaigneau et al., 2013) at this latitude.

The elevated poleward velocities were most likely caused by a downwelling CTW. Satellite SLA data indicate a positive anomaly propagating eastward from the eastern equatorial Pacific to the South American coast and subsequently poleward to beyond 14° S. An elevated westerly wind anomaly on the equator in the central Pacific that occurred in April 2017 is suggested to have excited the initial Kelvin wave. Wind stress and wind stress curl variability along the South American coast did not impact the CTW nor the elevated alongshore velocities. The phase speed of the SLA signal propagation along the South

American coast is consistent with a first vertical mode CTW. Similarly, the vertical distribution of the poleward velocity anomaly at the eastern boundary generally agreed with the cross-shore-depth velocity structure of a first mode CTW.

While temperature and salinity conditions remained almost unaltered, the enhanced poleward water mass advection due to the CTW induced changes in the distribution of oxygen and nutrient along the eastern boundary. Below 100m depth, oxygen concentrations increased and the upper boundary of anoxic water ($O_2 > 2$ µmol kg^{-1}) deepened by about 50m due to both, the downward displacement of the isopycnals in the thermocline and the advection of ESSW having higher oxygen concentrations. Similarly, nitrate concentrations increased during the period of intensified poleward flow while phosphate concentrations and nitrogen deficit decreased (Fig. 12).

Similar to our results, previous studies have identified the first vertical mode CTWs to dominate intraseasonal variability in the eastern South Pacific based on tide gauge and SLA observations (e.g. Brink, 1982; Shaffer et al., 1997) and model results (Illig et al., 2018b). However, there is disagreement in the details of the observed cross-shore-depth alongshore velocity structure of the CTW and the velocity structure of first vertical mode solution of a linear wave model using local stratification and topography suggesting that additional dynamical processes are important.

A possible explanation of the poor agreement is interaction of the CTW with local topography. North of our sampling site, the continental slope bends offshore at depths between 500 m to 1000 m (Fig. 1, insert) while the shelf narrows to the south. Changes in coastline, shelf width, and along-slope bathymetry lead to a transfer of CTW energy into higher modes (scattering) and upstream backscattering (Wang, 1980; Wilkin and Chapman, 1990; Kämpf, 2018; Brunner et al., 2019). The influence of changes in shelf width on the upstream alongshore flow structure can extend to 200 km upstream (Wilkin and Chapman, 1990) but, due to relative smooth downstream topography, is likely not relevant here. However, the bent of the continental slope and other topographic irregularities north of our sampling site may stimulate energy transfer into high vertical mode CTWs. In turn, the superposition of several vertical modes could explain the observed elevated poleward flow between 50 m and 300 m depth (Fig. 3 and 12) that cannot be explained by a first mode CTW. In fact, a recent model study suggests that differences between the theoretical CTW solutions and observations are predominately due to wave scattering (Brunner et al., 2019).

The temperature and salinity conditions on the shelf remain almost unchanged despite the strongly intensified poleward flow, suggesting that the same water mass was advected within the boundary current regime during both observational periods. However, during the presence of the CTW, SSTs were lower than in the period prior to the wave. This is a somewhat unexpected result because downwelling CTW weaken coastal upwelling due to the downward displacement of the thermocline which should lead to warmer SSTs and earlier in March 2017 downwelling CTWs contributed to the anomalously high SST in the coastal El Niño (Echevin et al., 2018; Peng et al., 2019). However, previous studies have shown that the impact of CTWs on intraseasonal SST variability off Peru is limited (Dewitte et al., 2011; Illig et al., 2014). Specifically, in May 2017 SST reduction agrees with both the seasonal cycle (Graco et al., 2017) and the decline of the warm Coastal El Niño with peak SST in March (e.g. Garreaud, 2018).

Changes in oxygen concentrations due to the CTW event were rather small. In the water column between 100 m and 200 m depth, oxygen concentrations increased by 1 to 10 µmol kg^{-1}, only. However, the limited impact of the CTW on the oxygen distribution is likely related to high oxygen concentrations present at the study site before the wave passage. Previous measurement programs in this area found the mean depth of the upper boundary of the OMZ on the shelf at about 50 m depth (Gutiérrez et al., 2008; Dale et al., 2015, Graco et al., 2017) but deepening to 200 m or more during ENSO years (e.g. Levin et al., 2002; Espinoza-Morriberón et al., 2019). In particular, Dale et al. (2015) found oxygen levels below the detection limit between 30 and 400 m depth during previous measurement programs along 12° S. It is thus likely that the prevailing elevated oxygen concentrations are related to the Coastal El Niño event in the same way that canonical El Niños are related to enhanced oxygenation (Helly and Levin, 2004; Espinoza-Morriberón et al., 2019). Despite small oxygen concentration changes, the upper boundary of anoxic water deepened by about 50 m during the presence of the CTW (Fig. 12). The change from anoxic conditions to suboxic conditions with oxygen concentrations ($O_2 > 2$ µmol kg^{-1}) has important consequences for

biogeochemical processes and the benthic and pelagic communities (e.g. Gutiérrez et al., 2008). This study thus confirms previous suggestions that CTW lead to episodic oxygenation events that are vital for colonization of invertebrates and other biota within the predominately anoxic regions of the benthos and the water column above.

445   The increase in nitrate concentrations and the reduced nitrogen deficit are likely caused by the faster advection during the intensified flow period. The nitrate concentrations in the ESSW increase and waters with the same T-S properties are richer in nitrate following the intensification of the PCUC (Fig. 10), indicating the nitrate increase was not due to a different source of advected water. Along the ESSW pathway within the PCUC from the equator to 12° S, the nitrogen deficit increases while nitrate concentrations decrease (Silva et al., 2009; Zamora et al., 2012; Kalvelage et al., 2013). The resulting nitrogen deficit

450   accumulates with time during the poleward advection. Thus, an intensified PCUC increases the poleward advection of water with a lower nitrogen deficit. This can be verified by investigating the advection timescales. The alongshore distance from the equator to the 12° S (1800 km) and a PCUC velocity of 0.4 m s^{-1} yields a time scale of 52 days, while a time scale of 160 days results from a velocity of 0.13 m s^{-1} representing maximum climatological velocity (Chaigneau et al., 2013). Using a rate for N-loss of 48 nmol N l^{-1} d^{-1} (combined anammox and denitrification rates in the coastal OMZ from Kalvelage et al. (2013))

455   results in an N-loss difference of 5.2 µmol N l^{-1} due to the lower flow velocities. Indeed, the reduction of the nitrogen deficit by about 5 µmol N kg^{-1}, as observed throughout much of the PCUC core during the presence of the CTW, closely relates to this estimate. The sediments off Peru subjected to oxygen depleted bottom waters, release phosphate into the water column (Noffke et al., 2012; Lomnitz et al., 2016) that also contributes to the nitrogen deficit. Faster advection leads to a reduced accumulation of phosphate that is released from the sediments with lower phosphate concentrations during the strong PCUC

460   flow. However, the increase of nitrate exceeds the phosphate decrease by about 5 to 0.1 µmol kg^{-1}, a ratio higher than the nitrogen to phosphorus ratio given in equation 1. Therefore, changes of nitrate concentration dominate the reduction of the nitrogen deficit.

The increase in nitrate by the downwelling CTW implies that the change in alongshore advection with the increased flow is more important for the nitrate balance than downwelling. The downwelling would displace the nutricline and thus transfer low nutrient surface waters downwards, lowering nutrient concentrations, which was not observed. The decline in nitrate

465   concentrations during El Niño events has been associated with a nutricline displacement due to downwelling CTWs on interannual timescales (Graco et al., 2017; Espinoza-Morriberón et al., 2017). However, focusing on intraseasonal timescales, Echevin et al. (2014) modelled an almost cancelling of horizontal and vertical (i.e. nutricline movement) advection and a fast mode CTW not impacting nutricline depth. In a model study in the Atlantic Ocean, where nitrate decreases poleward as well,

470   it was shown that the total effect of CTWs on nitrate concentrations varies regionally due to a different balance of horizontal and vertical advection, but the horizontal advection always led to an increase in nitrate (Bachèlery et al., 2016).

The changes in redox state in the water column and especially bottom waters affect the biogeochemical cycling in the sediment as well. Because microbial storage of nitrate and nitrite by microorganisms in the sediment can sustain vigorous N turnover even in the absence of bottom water nitrate and nitrite (Dale et al., 2016; Sommer et al., 2016), episodic events of nitrogen

475   supply can be associated with continuous benthic nitrogen cycling. The absence of nitrate supply due to the absence of CTWs over longer time periods favours the depletion of nitrate in the water column as observed by Sommer et al. (2016) and may lead ultimately to the development of sulfidic events (Schunck et al., 2013; Dale et al., 2016; Callbeck et al., 2018).

6 Conclusion

Based on extensive physical and biogeochemical sampling, we describe and analyse the evolution of circulation, hydrography

480   and biogeochemistry off Peru in 2017. Poleward velocities within the PCUC intensified in May 2017 to several times the reported climatological mean. This increased flow occurs during a limited time period in May in between weaker poleward transport in April and late June. The propagation velocity of positive SLA along the equator and coastline suggests that the

intensified current is caused by a poleward propagating downwelling CTW of the first baroclinic mode forced around 160° W at the equator that caused a positive SLA signal east of 95° W. The transition of the circulation from a weak poleward flow to strong poleward flow decreased the timescale of alongshore advection from the equatorial current regime to the study site at 12° S.

The downwelling CTW is not associated with strong vertical displacements of waters; instead the advection caused by the intensified PCUC is more important. For parameters without strong horizontal gradients, an increase in PCUC flow does not cause pronounced changes in the advection. In this study this applied to the conservative properties of temperature and salinity as well as for oxygen where alongshore gradients are weak (Zamora et al., 2012). For these parameters there are no large differences between both circulation phases that can be attributed clearly to the altered circulation. Yet concentrations of nutrients are influenced by shorter transit times, being less altered by biogeochemical cycling. This leads to an increase of bioavailable nitrogen in the OMZ (Fig. 12) and its biogeochemistry is strongly changed by the increased ratio of nitrogen to phosphorus related to the increased advection.

For the period from April to May 2017, our study suggests an increase in nitrate levels due to the passage of an intraseasonal downwelling CTW. This contrasts with the decrease observed previously on interannual timescales caused by downwelling CTWs (Graco et al., 2017). This shows that the impact of CTWs on nutrient biogeochemistry is a complex balance between different factors, with potentially different outcome on different timescales. Analysing the processes associated with individual intraseasonal waves is also necessary to understand the interannual effect of CTWs, which is based on varying occurrence of such waves in different years.

The high variability of circulation, nutrients and the nitrogen deficit demonstrates the need for temporally resolved sampling as an individual section recorded may be very different from the situation a few weeks later. Quantification of intraseasonal variability in CTWs and their impact is – other than in modelling studies (e.g. Echevin et al., 2014) – only possible by sampling at high temporal resolution.

Data availability

Ship based observations are available at PANGAEA (https://doi.pangaea.de/10.1594/PANGAEA.903828). Global Ocean Gridded L4 sea surface heights are made available by E.U. Copernicus Marine Service (CMEMS). NOAA ERSSTv5 data are made available by the NOAA National Centers for Environmental Information. ASCAT data were obtained from the Centre de Recherche et d'Exploitation Satellitaire (CERSAT), at IFREMER, Plouzané (France).

Author contributions

JL carried out the data analysis and wrote the main manuscript. JL conceived the study with MD and with input by DC, ST and MV. MD and SS lead the observational program at sea. GK calibrated and processed the CTD. AD and SS provided the nutrient data. EA provided the ammonium data. All co-authors reviewed the manuscript and contributed to the scientific interpretation and discussion.

Competing Interests

The authors declare that they have no conflict of interest.

Acknowledgements

This study was funded by the Deutsche Forschungsgemeinschaft as part of the Sonderforschungsbereich 754 "Climate–Biogeochemistry Interactions in the Tropical Ocean". ST received funding by the European Commission (Horizon 2020 programme, MSCA-IF-2016, proposal number WACO 749699: Fine-scale Physics, Biogeochemistry and Climate Change in the West African Coastal Ocean). We thank the Peruvian authorities for the permission to carry out scientific work in their national waters. We thank the captains and the crew of R/V Meteor for their support during the cruises. We thank Regina Surberg and Bettina Domeyer for the nutrient analysis, all other people involved in the measurement program and Rena Czeschel for post-cruise processing of the vmADCP data. We thank two anonymous reviewers for their helpful suggestions. Many figures in this study use colour maps from the cmocean package (Thyng et al., 2016). Global Ocean Gridded L4 sea surface heights were made available by E.U. Copernicus Marine Service (CMEMS).

References

Albert, A., Echevin, V., Lévy, M., and Aumont, O.: Impact of nearshore wind stress curl on coastal circulation and primary productivity in the Peru upwelling system, J. Geophys. Res. Oceans, 115. doi:10.1029/2010JC006569, 2010.

Bachèlery, M.-L., Illig, S., and Dadou, I.: Forcings of nutrient, oxygen, and primary production interannual variability in the southeast Atlantic Ocean, Geophys. Res. Lett., 43, 8617-8625. doi:10.1002/2016gl070288, 2016.

Bakun, A. and Nelson, C. S.: The Seasonal Cycle of Wind-Stress Curl in Subtropical Eastern Boundary Current Regions, J. Phys. Oceanogr., 21, 1815-1834. doi:10.1175/1520-0485(1991)021<1815:TSCOWS>2.0.CO;2, 1991.

Becker, J. J., Sandwell, D. T., Smith, W. H. F., Braud, J., Binder, B., Depner, J., Fabre, D., Factor, J., Ingalls, S., Kim, S.-H., Ladner, R., Marks, K., Nelson, S., Pharaoh, A., Trimmer, R., Rosenberg, J. V., Wallace, G. and Weatherall, P.: Global Bathymetry and Elevation Data at 30 Arc Seconds Resolution: SRTM30_PLUS, Marine Geodesy, 32(4), 355–371, doi:10.1080/01490410903297766, 2009.

Belmadani, A., Echevin, V., Dewitte, B., and Colas, F.: Equatorially forced intraseasonal propagations along the Peru-Chile coast and their relation with the nearshore eddy activity in 1992–2000: A modeling study, J. Geophys. Res. Oceans, 117. doi:10.1029/2011JC007848, 2012.

Bentamy, A. and Fillon, D. C.: Gridded surface wind fields from Metop/ASCAT measurements, Int. J. Remote Sens., 33, 1729-1754. doi:10.1080/01431161.2011.600348, 2012.

Brandt, P., Bange, H. W., Banyte, D., Dengler, M., Didwischus, S.-H., Fischer, T., Greatbatch, R. J., Hahn, J., Kanzow, T., Karstensen, J., Körtzinger, A., Krahmann, G., Schmidtko, S., Stramma, L., Tanhua, T., and Visbeck, M.: On the role of circulation and mixing in the ventilation of oxygen minimum zones with a focus on the eastern tropical North Atlantic, Biogeosciences, 12, 489-512. doi:10.5194/bg-12-489-2015, 2015.

Brink, K. H.: A Comparison of Long Coastal Trapped Wave Theory with Observations off Peru, J. Phys. Oceanogr., 12, 897-913. doi:10.1175/1520-0485(1982)012<0897:ACOLCT>2.0.CO;2, 1982.

Brink, K. H.: Energy Conservation in Coastal-Trapped Wave Calculations, J. Phys. Oceanogr., 19, 1011-1016. doi:10.1175/1520-0485(1989)019<1011:ECICTW>2.0.CO;2, 1989.

Brink, K. H.: Stable coastal-trapped waves with stratification, topography and mean flow, MBLWHOI Library. doi:10.1575/1912/10527, 2018.

Brink, K. H. and Chapman, D. C.: Programs for computing properties of coastal-trapped waves and wind-driven motions over the continental shelf and slope, WHOI Technical Reports, Woods Hole Oceanographic Institution. doi:10.1575/1912/5368, 1987.

Brink, K. H., Halpern, D. and Smith, R. L.: Circulation in the Peruvian upwelling system near 15°S, J. Geophys. Res., 85(C7), 4036–4048, doi:10.1029/jc085ic07p04036, 1980.

Brink, K. H., Halpern, D., Huyer, A., and Smith, R. L.: The physical environment of the Peruvian upwelling system, Prog. Oceanogr., 12, 285-305. doi:10.1016/0079-6611(83)90011-3, 1983.

560 Brunner, K., Rivas, D. and Lwiza, K. M. M.: Application of Classical Coastal Trapped Wave Theory to High-Scattering Regions, J. Phys. Oceanogr., 49(9), 2201–2216, doi:10.1175/JPO-D-18-0112.1, 2019.

Callbeck, C. M., Lavik, G., Ferdelman, T. G., Fuchs, B., Gruber-Vodicka, H. R., Hach, P. F., Littmann, S., Schoffelen, N. J., Kalvelage, T., Thomsen, S., Schunck, H., Löscher, C. R., Schmitz, R. A., and Kuypers, M. M. M.: Oxygen minimum zone cryptic sulfur cycling sustained by offshore transport of key sulfur oxidizing bacteria, Nat. Commun., 9. doi:10.1038/s41467-

565 018-04041-x, 2018.

Carr, M.-E.: Estimation of potential productivity in Eastern Boundary Currents using remote sensing, Deep Sea Res. Part II, 49, 59-80. doi:10.1016/S0967-0645(01)00094-7, 2002.

Chaigneau, A., Dominguez, N., Eldin, G., Vasquez, L., Flores, R., Grados, C., and Echevin, V.: Near-coastal circulation in the Northern Humboldt Current System from shipboard ADCP data, J. Geophys. Res. Oceans, 118, 5251-5266.

570 doi:10.1002/jgrc.20328, 2013.

Chang, B. X., Devol, A. H., and Emerson, S. R.: Denitrification and the nitrogen gas excess in the eastern tropical South Pacific oxygen deficient zone, Deep Sea Res. Part I, 57, 1092-1101. doi:10.1016/j.dsr.2010.05.009, 2010.

Chavez, F. P., Bertrand, A., Guevara-Carrasco, R., Soler, P., and Csirke, J.: The northern Humboldt Current System: Brief history, present status and a view towards the future, Prog. Oceanogr., 79, 95-105. doi:10.1016/j.pocean.2008.10.012, 2008.

575 Dale, A. W., Graco, M., and Wallmann, K.: Strong and Dynamic Benthic-Pelagic Coupling and Feedbacks in a Coastal Upwelling System (Peruvian Shelf), Front. Mar. Sci. 4:29, doi.org/10.3389/fmars.2017.00029, 2017.

Dale, A. W., Sommer, S., Lomnitz, U., Montes, I., Treude, T., Liebetrau, V., Gier, J., Hensen, C., Dengler, M., Stolpovsky, K., Bryant, L. D. and Wallmann, K.: Organic carbon production, mineralisation and preservation on the Peruvian margin, Biogeosciences, 12(5), 1537–1559, doi:10.5194/bg-12-1537-2015, 2015.

580 Dale, A. W., Sommer, S., Lomnitz, U., Bourbonnais, A., and Wallmann, K.: Biological nitrate transport in sediments on the Peruvian margin mitigates benthic sulfide emissions and drives pelagic N loss during stagnation events, Deep Sea Res. Part I, 112, 123-136. doi:10.1016/j.dsr.2016.02.013, 2016.

Dengler, M. and Sommer, S.: Coupled benthic and pelagic oxygen, nutrient and trace metal cycling, ventilation and carbon degradation in the oxygen minimum zone of the Peruvian continental margin (SFB 754): Cruise No. M 136 11.04. - 03.05.2017

585 Callao (Peru) - Callao Solute-Flux Peru I, METEOR-Berichte, doi:10.3289/CR_M136, 2017.

Dewitte, B., Illig, S., Renault, L., Goubanova, K., Takahashi, K., Gushchina, D., Mosquera, K. and Purca, S.: Modes of covariability between sea surface temperature and wind stress intraseasonal anomalies along the coast of Peru from satellite observations (2000–2008), J. Geophys. Res. Oceans, 116(C4), doi:10.1029/2010JC006495, 2011.

Echevin, V., Albert, A., Lévy, M., Graco, M., Aumont, O., Piétri, A., and Garric, G.: Intraseasonal variability of nearshore

590 productivity in the Northern Humboldt Current System: The role of coastal trapped waves, Cont. Shelf Res., 73, 14-30. doi:10.1016/j.csr.2013.11.015, 2014.

Echevin, V., Colas, F., Espinoza-Morriberon, D., Vasquez, L., Anculle, T., and Gutierrez, D.: Forcings and Evolution of the 2017 Coastal El Niño Off Northern Peru and Ecuador, Front. Mar. Sci., 5, 367. doi:10.3389/fmars.2018.00367, 2018.

Enfield, D. B., Cornejo-Rodriguez, M. D., Smith, R. L., and Newberger, P. A.: The equatorial source of propagating variability

595 along the Peru coast during the 1982–1983 El Niño, J. Geophys. Res. Oceans, 92, 14335-14346. doi:10.1029/JC092iC13p14335, 1987.

Espinoza-Morriberón, D., Echevin, V., Colas, F., Tam, J., Gutierrez, D., Graco, M., Ledesma, J. and Quispe-Ccalluari, C.: Oxygen Variability During ENSO in the Tropical South Eastern Pacific, Front. Mar. Sci., 5, 526, doi:10.3389/fmars.2018.00526, 2019.

600   Espinoza-Morriberón, D., Echevin, V., Colas, F., Tam, J., Ledesma, J., Vásquez, L., and Graco, M.: Impacts of El Niño events on the Peruvian upwelling system productivity, J. Geophys. Res. Oceans. doi:10.1002/2016JC012439, 2017.

Fennel, W., Junker, T., Schmidt, M. and Mohrholz, V.: Response of the Benguela upwelling systems to spatial variations in the wind stress, Cont. Shelf Res., 45, 65–77, doi:10.1016/j.csr.2012.06.004, 2012.

Fischer, J., Brandt, P., Dengler, M., Müller, M., and Symonds, D.: Surveying the Upper Ocean with the Ocean Surveyor: A
605   New Phased Array Doppler Current Profiler, J. Atmos. Oceanic Technol., 20, 742-751. doi:10.1175/1520-0426(2003)20<742:STUOWT>2.0.CO;2, 2003.

Garreaud, R. D.: A plausible atmospheric trigger for the 2017 coastal El Niño, Int. J. Climatol., 38, e1296-e1302. doi:10.1002/joc.5426, 2018.

Graco, M. I., Purca, S., Dewitte, B., Castro, C. G., Morón, O., Ledesma, J., Flores, G. and Gutiérrez, D.: The OMZ and nutrient
610   features as a signature of interannual and low-frequency variability in the Peruvian upwelling system, Biogeosciences, 14(20), 4601–4617, doi:10.5194/bg-14-4601-2017, 2017.

Grados, C., Chaigneau, A., Echevin, V., and Dominguez, N.: Upper ocean hydrology of the Northern Humboldt Current System at seasonal, interannual and interdecadal scales, Prog. Oceanogr., 165, 123-144. doi:10.1016/j.pocean.2018.05.005, 2018.

615   Grasshoff, K., Kremling, K. and Ehrhardt, M.: Methods of seawater analysis, John Wiley & Sons., 1983.

Gruber, N.: The marine nitrogen cycle: overview and challenges, in Nitrogen in the marine environment, vol. 2, edited by D. G. Capone, D. A. Bronk, M. Mulholland, and E. J. Carpenter, pp. 1–50, Elsevier Amsterdam., 2008.

Gruber, N. and Sarmiento, J. L.: Global patterns of marine nitrogen fixation and denitrification, Global Biogeochem. Cycles, 11, 235-266. doi:10.1029/97GB00077, 1997

620   Gruber, N. and Sarmiento, J. L.: Large-scale biogeochemical-physical interactions in elemental cycles, in THE SEA: Biological–Physical Interactions in the Oceans, vol. 12, edited by A. R. Robinson, J. J. McCarthy, and B. J. Rothschild, pp. 337–399, Wiley, New York., 2002.

Gunther, E. R.: A report on oceanographical investigations in the Peru Coastal Current, Discovery Rep., 13, 107–276, 1936.

Gutiérrez, D., Enríquez, E., Purca, S., Quipúzcoa, L., Marquina, R., Flores, G. and Graco, M.: Oxygenation episodes on the
625   continental shelf of central Peru: Remote forcing and benthic ecosystem response, Prog. Oceanogr., 79(2–4), 177–189, doi:10.1016/j.pocean.2008.10.025, 2008.

Hauschildt, J., Thomsen, S., Echevin, V., Oschlies, A., José, Y. S., Krahmann, G., Bristow, L. A. and Lavik, G.: The fate of upwelled nitrate off Peru shaped by submesoscale filaments and fronts, Biogeosci. Discuss., 1–32, doi:10.5194/bg-2020-112, in review, 2020.

630   Helly, J. J. and Levin, L. A.: Global distribution of naturally occurring marine hypoxia on continental margins, Deep Sea Res. Part I, 51, 1159-1168. doi:10.1016/j.dsr.2004.03.009, 2004.

Hill, A. E., Hickey, B. M., Shillington, F. A., Strub, P. T., Brink, K. H., Barton, E. D. and Thomas, A. C.: Eastern Ocean Boundaries, in The Seas: The Global Coastal Ocean, vol. 11, edited by A. R. Robinson and K. H. Brink, pp. 29–68, John Wiley, New York., 1998.

635   Holmes, R. M., Aminot, A., Kérouel, R., Hooker, B. A., and Peterson, B. J.: A simple and precise method for measuring ammonium in marine and freshwater ecosystems, Can. J. Fish. Aquat.Sci., 56, 1801-1808. doi:10.1139/f99-128, 1999.

Hood, E. M., Sabine, C. L. and Sloyan, B. M.: The GO-SHIP Repeat Hydrography Manual: a collection of expert reports and guidelines, Version 1, IOCCP Report 14., ICPO Publication Series 134., 2010.

Hormazabal, S., Shaffer, G., and Pizarro, O.: Tropical Pacific control of intraseasonal oscillations off Chile by way of oceanic
640   and atmospheric pathways, Geophys. Res. Lett., 29. doi:10.1029/2001GL013481, 2002.

Huang, B., Thorne, P. W., Banzon, V. F., Boyer, T., Chepurin, G., Lawrimore, J. H., Menne, M. J., Smith, T. M., Vose, R. S. and Zhang, H.-M.: NOAA Extended Reconstructed Sea Surface Temperature (ERSST), Version 5, doi:10.7289/V5T72FNM, 2017a.

Huang, B., Thorne, P. W., Banzon, V. F., Boyer, T., Chepurin, G., Lawrimore, J. H., Menne, M. J., Smith, T. M., Vose, R. S.

645 and Zhang, H.-M.: Extended Reconstructed Sea Surface Temperature, Version 5 (ERSSTv5): Upgrades, Validations, and Intercomparisons, J. Climate, 30(20), 8179–8205, doi:10.1175/JCLI-D-16-0836.1, 2017b.

Illig, S., Bachèlery, M.-L., and Cadier, E.: Subseasonal Coastal-Trapped Wave Propagations in the Southeastern Pacific and Atlantic Oceans: 2. Wave Characteristics and Connection With the Equatorial Variability, J. Geophys. Res. Oceans, 123, 3942-3961. doi:10.1029/2017JC013540, 2018b.

650 Illig, S., Cadier, E., Bachèlery, M.-L., and Kersalé, M.: Subseasonal Coastal-Trapped Wave Propagations in the Southeastern Pacific and Atlantic Oceans: 1. A New Approach to Estimate Wave Amplitude, J. Geophys. Res. Oceans, 123, 3915-3941. doi:10.1029/2017JC013539, 2018a

Illig, S., Dewitte, B., Goubanova, K., Cambon, G., Boucharel, J., Monetti, F., Romero, C., Purca, S. and Flores, R.: Forcing mechanisms of intraseasonal SST variability off central Peru in 2000–2008, J. Geophys. Res. Oceans, 119(6), 3548–3573,

655 doi:10.1002/2013JC009779, 2014.

IOC, SCOR and IAPSO: The international thermodynamic equation of seawater – 2010: Calculation and use of thermodynamic properties, edited by U. (english), Intergovernmental Oceanographic Commission., 2010.

Junker, T., Schmidt, M. and Mohrholz, V.: The relation of wind stress curl and meridional transport in the Benguela upwelling system, J. Mar. Syst., 143, 1–6, doi:10.1016/j.jmarsys.2014.10.006, 2015.

660 Kalvelage, T., Lavik, G., Lam, P., Contreras, S., Arteaga, L., Löscher, C. R., Oschlies, A., Paulmier, A., Stramma, L. and Kuypers, M. M.: Nitrogen cycling driven by organic matter export in the South Pacific oxygen minimum zone, Nat. Geosci., 6(3), 228–234, doi:10.1038/ngeo1739, 2013.

Kämpf, J.: On the Dynamics of Canyon-Flow Interactions, Journal of Marine Science and Engineering, 6(4), doi:10.3390/jmse6040129, 2018.

665 Kämpf, J. and Chapman, P.: Upwelling Systems of the World: A Scientific Journey to the Most Productive Marine Ecosystems, Springer, 2016.

Karstensen, J., Schütte, F., Pietri, A., Krahmann, G., Fiedler, B., Grundle, D., Hauss, H., Körtzinger, A., Löscher, C. R., Testor, P., Vieira, N. and Visbeck, M.: Upwelling and isolation in oxygen-depleted anticyclonic modewater eddies and implications for nitrate cycling, Biogeosciences, 14(8), 2167–2181, doi:10.5194/bg-14-2167-2017, 2017.

670 Klenz, T., Dengler, M., and Brandt, P.: Seasonal Variability of the Mauritania Current and Hydrography at 18° N, J. Geophys. Res. Oceans, 123, 8122-8137. doi:10.1029/2018jc014264, 2018.

Kuypers, M. M. M., Lavik, G., Woebken, D., Schmid, M., Fuchs, B. M., Amann, R., Jørgensen, B. B. and Jetten, M. S. M.: Massive nitrogen loss from the Benguela upwelling system through anaerobic ammonium oxidation, Proceedings of the National Academy of Sciences, 102(18), 6478–6483, doi:10.1073/pnas.0502088102, 2005.

675 Lam, P., Lavik, G., Jensen, M. M., van de Vossenberg, J., Schmid, M., Woebken, D., Gutiérrez, D., Amann, R., Jetten, M. S. M. and Kuypers, M. M. M.: Revising the nitrogen cycle in the Peruvian oxygen minimum zone, Proceedings of the National Academy of Sciences, 106(12), 4752–4757, doi:10.1073/pnas.0812444106, 2009.

Leth, O. and Middleton, J. F.: A numerical study of the upwelling circulation off central Chile: Effects of remote oceanic forcing, J. Geophys. Res. Oceans, 111(C12), doi:10.1029/2005JC003070, 2006.

680 Lomnitz, U., Sommer, S., Dale, A. W., Löscher, C. R., Noffke, A., Wallmann, K., and Hensen, C.: Benthic phosphorus cycling in the Peruvian oxygen minimum zone, Biogeosciences, 13, 1367-1386. doi:10.5194/bg-13-1367-2016, 2016.

Levin, L., Gutiérrez, D., Rathburn, A., Neira, C., Sellanes, J., Muñoz, P., Gallardo, V. and Salamanca, M.: Benthic processes on the Peru margin: a transect across the oxygen minimum zone during the 1997–98 El Niño, Prog. Oceanogr., 53(1), 1–27, doi:10.1016/S0079-6611(02)00022-8, 2002.

685 Marchesiello, P., McWilliams, J. C. and Shchepetkin, A.: Equilibrium Structure and Dynamics of the California Current System, J. Phys. Oceanogr., 33(4), 753–783, doi: 10.1175/1520-0485(2003)33<753:ESADOT>2.0.CO;2, 2003.

McCreary, J. P. and Chao, S.-Y.: Three-dimensional shelf circulation along an eastern ocean boundary, J. Mar. Res., 43, 13-36. doi:10.1357/002224085788437316, 1985.

McDougall, T. J. and Barker, P. M.: Getting started with TEOS-10 and the Gibbs Seawater (GSW) oceanographic toolbox,
690 SCOR/IAPSO WG 127, 2011.

Montes, I., Colas, F., Capet, X., and Schneider, W.: On the pathways of the equatorial subsurface currents in the eastern equatorial Pacific and their contributions to the Peru-Chile Undercurrent, J. Geophys. Res. Oceans, 115. doi:10.1029/2009JC005710, 2010.

Moore, D. W. and Philander, S. G. H.: Modelling of the tropical ocean circulation, in The Sea, vol. 6, pp. 316–361, John
695 Wiley., 1977.

Noffke, A., Hensen, C., Sommer, S., Scholz, F., Bohlen, L., Mosch, T., Graco, M. and Wallmann, K.: Benthic iron and phosphorus fluxes across the Peruvian oxygen minimum zone, Limnol. Oceanogr., 57(3), 851–867, doi:10.4319/lo.2012.57.3.0851, 2012.

Pennington, J. T., Mahoney, K. L., Kuwahara, V. S., Kolber, D. D., Calienes, R., and Chavez, F. P.: Primary production in the
700 eastern tropical Pacific: A review, Prog. Oceanogr., 69, 285-317. doi:10.1016/j.pocean.2006.03.012, 2006.

Penven, P., Echevin, V., Pasapera, J., Colas, F., and Tam, J.: Average circulation, seasonal cycle, and mesoscale dynamics of the Peru Current System: A modeling approach, J. Geophys. Res. Oceans, 110. doi:10.1029/2005JC002945, 2005.

Philander, S. G. H. and Yoon, J.-H.: Eastern Boundary Currents and Coastal Upwelling, J. Phys. Oceanogr., 12(8), 862–879, doi:10.1175/1520-0485(1982)012<0862:EBCACU>2.0.CO;2, 1982.

705 Pietri, A., Echevin, V., Testor, P., Chaigneau, A., Mortier, L., Grados, C., and Albert, A.: Impact of a coastal-trapped wave on the near-coastal circulation of the Peru upwelling system from glider data, J. Geophys. Res. Oceans, 119, 2109-2120. doi:10.1002/2013JC009270, 2014.

Pizarro, O., Shaffer, G., Dewitte, B., and Ramos, M.: Dynamics of seasonal and interannual variability of the Peru-Chile Undercurrent, Geophys. Res. Lett., 29, 22-1 - 22-4. doi:10.1029/2002GL014790, 2002.

710 Revsbech, N. P., Larsen, L. H., Gundersen, J., Dalsgaard, T., Ulloa, O., and Thamdrup, B.: Determination of ultra-low oxygen concentrations in oxygen minimum zones by the STOX sensor, Limnol. Oceanogr. Methods, 7, 371-381. doi:10.4319/lom.2009.7.371, 2009.

Romea, R. D. and Smith, R. L.: Further Evidence for Coastal Trapped Waves along the Peru Coast, J. Phys. Oceanogr., 13(8), 1341–1356, doi:10.1175/1520-0485(1983)013<1341:FEFCTW>2.0.CO;2, 1983.

715 Sakamoto, C. M., Johnson, K. S., and Coletti, L. J.: Improved algorithm for the computation of nitrate concentrations in seawater using an in situ ultraviolet spectrophotometer, Limnol. Oceanogr. Methods, 7, 132-143. doi:10.4319/lom.2009.7.132, 2009.

Schunck, H., Lavik, G., Desai, D. K., Großkopf, T., Kalvelage, T., Löscher, C. R., Paulmier, A., Contreras, S., Siegel, H., Holtappels, M., Rosenstiel, P., Schilhabel, M. B., Graco, M., Schmitz, R. A., Kuypers, M. M. M. and LaRoche, J.: Giant
720 Hydrogen Sulfide Plume in the Oxygen Minimum Zone off Peru Supports Chemolithoautotrophy, PLoS One, 8(8), 1–18, doi:10.1371/journal.pone.0068661, 2013.

Shaffer, G., Pizarro, O., Djurfeldt, L., Salinas, S., and Rutllant, J. (1997). Circulation and Low-Frequency Variability near the Chilean Coast: Remotely Forced Fluctuations during the 1991–92 El Niño, Journal of Physical Oceanography, 27, 217-235. doi:10.1175/1520-0485(1997)027<0217:CALFVN>2.0.CO;2, 1997.

725   Silva, N., Rojas, N., and Fedele, A.: Water masses in the Humboldt Current System: Properties, distribution, and the nitrate deficit as a chemical water mass tracer for Equatorial Subsurface Water off Chile, Deep Sea Res. Part II, 56, 1004-1020. doi:10.1016/j.dsr2.2008.12.013, 2009.

Sommer, S., Gier, J., Treude, T., Lomnitz, U., Dengler, M., Cardich, J., and Dale, A. W.: Depletion of oxygen, nitrate and nitrite in the Peruvian oxygen minimum zone cause an imbalance of benthic nitrogen fluxes, Deep Sea Res. Part I, 112, 113-

730   122. doi:10.1016/j.dsr.2016.03.001, 2016.

Sommer, S., Dengler, M. and Shipboard Scientific Party.: Benthic element cycling, fluxes and transport of nutrients and trace metals across the benthic boundary layer in the Peruvian oxygen minimum zone (SFB 754), Cruise No. 137, 06.05. - 29.05.2017, Callao (Peru) - Callao, METEOR-Berichte, doi:10.2312/cr_m137, 2019.

Strub, P. T., Mesias, J. M., Montecino, V., Rutllant, J. and Salinas, S.: Coastal ocean circulation off western South America,

735   in The Seas: The Global Coastal Ocean, vol. 11, edited by A. R. Robinson and K. H. Brink, pp. 273–313, John Wiley, New York., 1998.

Thomsen, S., Kanzow, T., Krahmann, G., Greatbatch, R. J., Dengler, M., and Lavik, G.: The formation of a subsurface anticyclonic eddy in the Peru-Chile Undercurrent and its impact on the near-coastal salinity, oxygen, and nutrient distributions, J. Geophys. Res. Oceans, 121, 476-501. doi:10.1002/2015JC010878, 2016.

740   Thomsen, S., Karstensen, J., Kiko, R., Krahmann, G., Dengler, M., and Engel, A.: Remote and local drivers of oxygen and nitrate variability in the shallow oxygen minimum zone off Mauritania in June 2014, Biogeosciences, 16, 979-998. doi:10.5194/bg-16-979-2019, 2019.

Thyng, K. M., Greene, C. A., Hetland, R. D., Zimmerle, H. M. and DiMarco, S. F.: True Colors of Oceanography: Guidelines for Effective and Accurate Colormap Selection, Oceanography, 29, doi:10.5670/oceanog.2016.66, 2016.

745   Ulloa, O., Canfield, D. E., DeLong, E. F., Letelier, R. M. and Stewart, F. J.: Microbial oceanography of anoxic oxygen minimum zones, Proceedings of the National Academy of Sciences, 109(40), 15996–16003, doi:10.1073/pnas.1205009109, 2012.

Wang, D.-P.: Diffraction of Continental Shelf Waves by Irregular Alongshore Geometry, J. Phys. Oceanogr., 10(8), 1187–1199, doi:10.1175/1520-0485(1980)010<1187:DOCSWB>2.0.CO;2, 1980.Wilkin, J. L. and Chapman, D. C.: Scattering of

750   Coastal-Trapped Waves by Irregularities in Coastline and Topography, J. Phys. Oceanogr., 20(3), 396–421, doi:10.1175/1520-0485(1990)020<0396:SOCTWB>2.0.CO;2, 1990.

Winkler, L. W.: Die Bestimmung des im Wasser gelösten Sauerstoffes, Ber. Dtsch. Chem. Ges., 21(2), 2843–2854, doi:10.1002/cber.188802102122, 1888.

Yoon, J.-H. and Philander, S. G. H.: The generation of coastal undercurrents, J. Oceanogr. Soc. Jpn., 38(4), 215–224,

755   doi:10.1007/bf02111104, 1982.

Yu, X., and McPhaden, M. J.: Seasonal Variability in the Equatorial Pacific, J. Phys. Oceanogr., 29, 925-947. doi:10.1175/1520-0485(1999)029<0925:SVITEP>2.0.CO;2, 1999.

Zamora, L. M., Oschlies, A., Bange, H. W., Huebert, K. B., Craig, J. D., Kock, A., and Löscher, C. R.: Nitrous oxide dynamics in low oxygen regions of the Pacific: insights from the MEMENTO database, Biogeosciences, 9, 5007-5022. doi:10.5194/bg-

760   9-5007-2012, 2012.

Table 1: Dates of R/V Meteor cruises conducted within the ETSP in 2017 including sampling time and number of CTD stations collected 12° S.

R/V Meteor cruise	Dates in 2017	Sampling duration along 12° S	CTD/nutrient stations at 12° S
M135	March 2 – April 8	2 days	
M136	April 18 – May 3	15 days	59 profiles
M137	May 6 – 29	23 days	92 profiles
M138	June 1 – July 5	1 day	
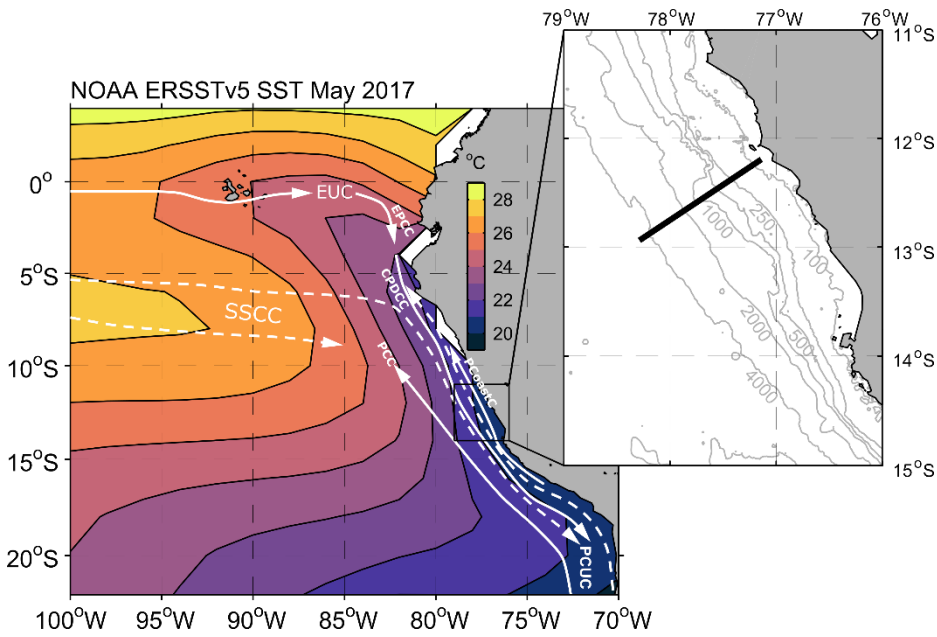
765

Figure 1: Sea surface temperature (NOAA ERSSTv5 SST) in the eastern tropical Pacific during May 2017 and schematic of the circulation. White solid lines indicate surface layer currents while dashed lines indicate thermocline layer currents (after Brandt et al., 2015). Abbreviated currents are the Equatorial Undercurrent (EUC), the Ecuador-Peru Coastal Current (EPCC), the Peru Coastal Current (PCoastC), the Peru Chile Current (PCC), the Southern Subsurface Countercurrents (SSCC, with two branches), the Chile–Peru Deep Coastal Current (CPDCC), and the Peru–Chile Undercurrent (PCUC). Figure insert shows the position of the 12° S section and local bathymetry (SRTM30 plus topography, Becker et al., 2009).
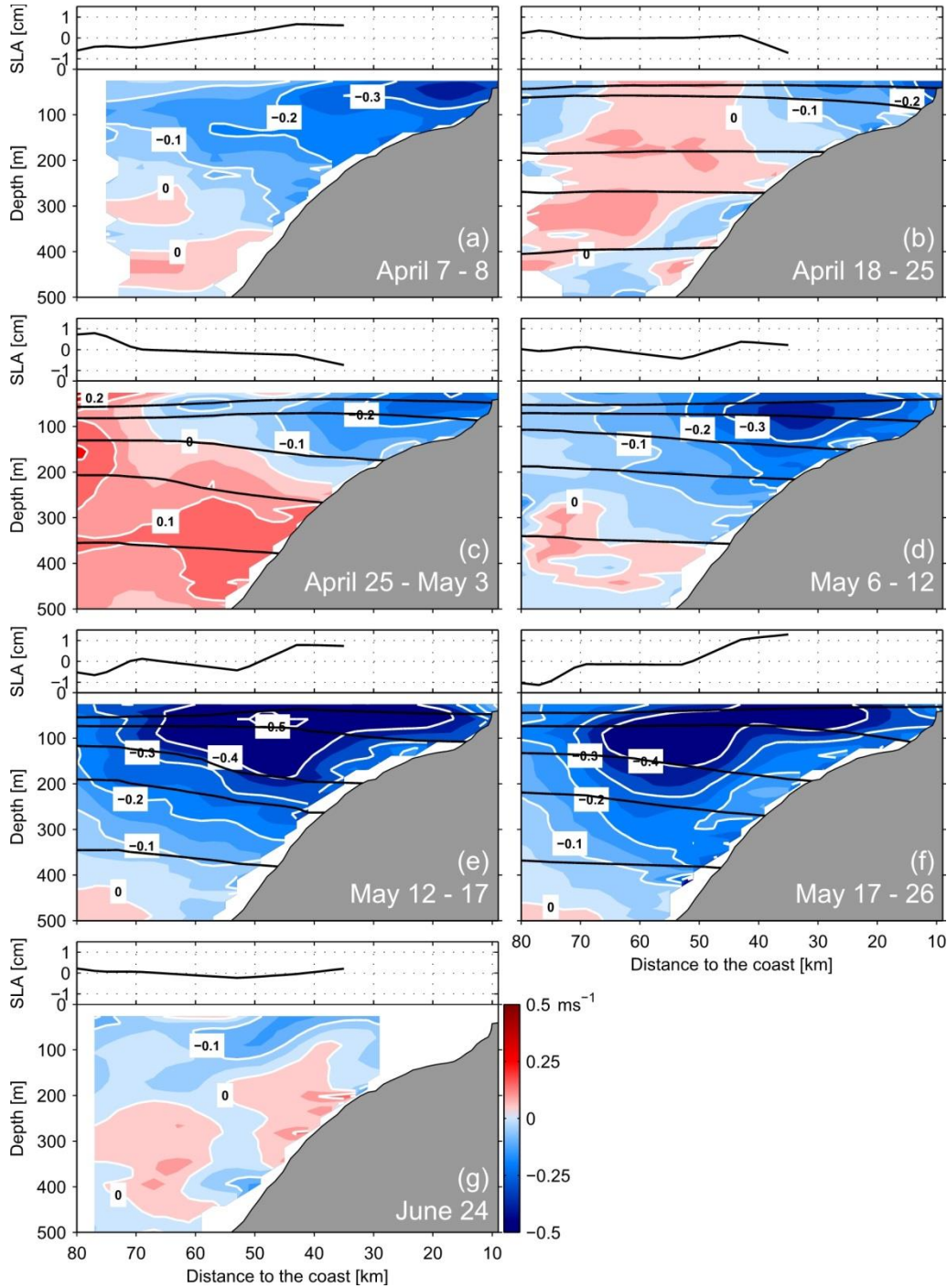
Figure 2: Depth-distance distribution of alongshore velocity (in m s⁻¹, positive equatorward, lower subpanels) and sea level anomaly (in cm, upper subpanels) at 12° S during April 7 – 8 (a), April 18 –25 (b), April 25 – May 3 (c), May 6 -12 (d), May 12 – 17 (e), May 17 – 26 (f) and June 24, 2017 (g). Black lines indicate the distribution of isopycnals (σθ) 25.6, 25.9, 26.2, 26.4, and 26.7 kg m⁻³.

795
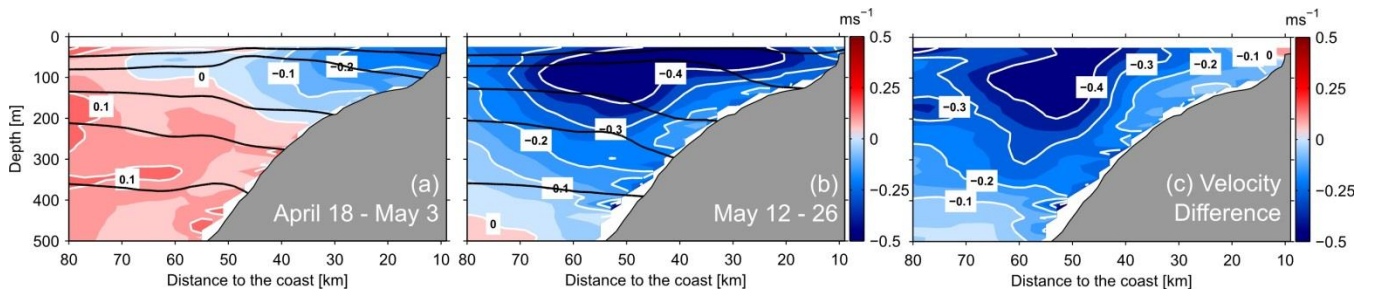
Figure 3: Depth - distance distribution of averaged alongshore velocity (positive equatorward) at 12° S prior to (a, April 18 – May
800 **3, 2017) and during (b, May 12 – 26, 2017) the PCUC intensification period. Panel c depicts the velocity difference between the two**
situations. Black lines indicate the distribution of isopycnals (σ$_\theta$) 25.6, 25.9, 26.2, 26.4, and 26.7 kg m^{-3}.
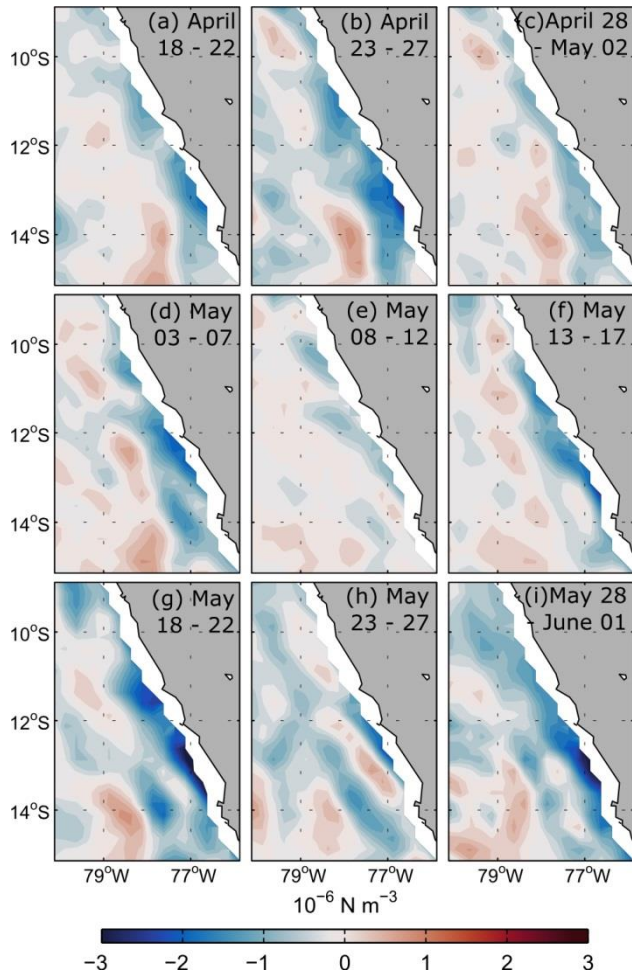
Figure 4: Five-day mean wind stress curl from ASCAT scatterometer winds off Peru during April 18 – 22 (a), April (23 – 27 (b), April 28 – May 02 (c), May 03 – 07 (d), May 08 – 12 (e), May 13 – 17 (f), May 18 – 22 (g), May 23 – 27 (h) and May 28 – June 01, 2017 (i).
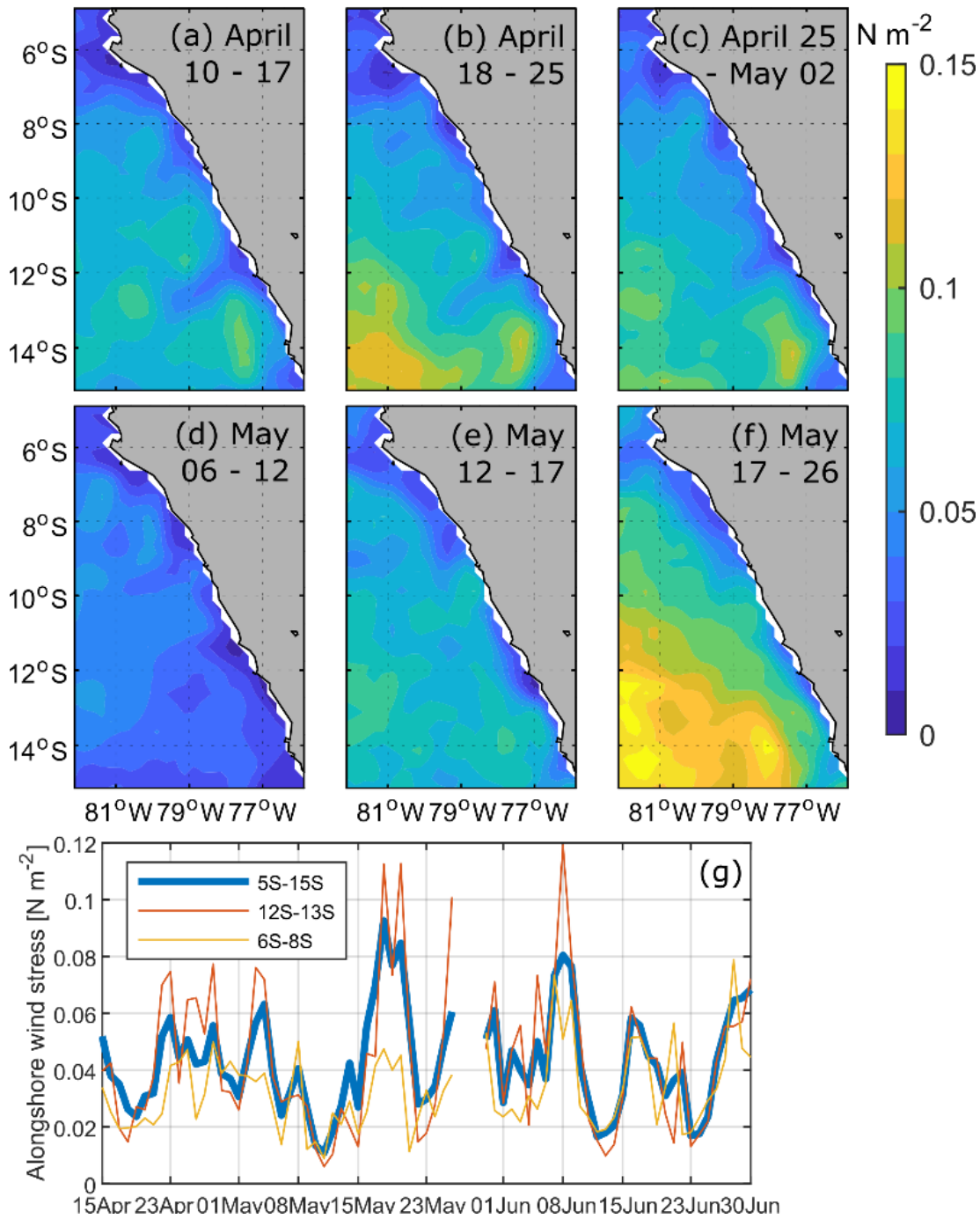
815

Figure 5: Weekly averages of alongshore wind stress from ASCAT scatterometer winds (upper two panel rows) for April 10 – 17 (a), April 18 -25 (b), April 25 – May 2 (c), May 06 – 12 (d), May 12 – 17 (e), May 17 – 26 (f). Lower panel (g) shows time series of alongshore wind stress averaged between 30 and 80 km from the coast for different bands of latitude.
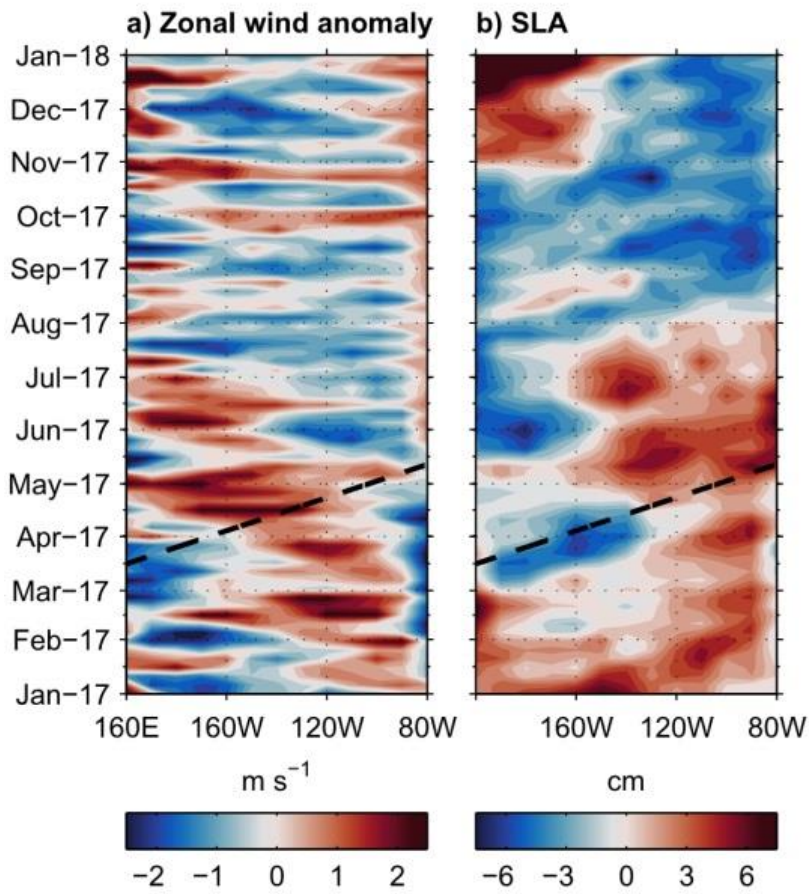
Figure 6: Hovmöller diagram of zonal wind anomaly (left panel) and SLA (right panel) along the central and eastern equatorial Pacific for the year 2017. The propagation of a first mode equatorial Kelvin wave is indicated by the dashed black line (phase speed 2.7 m s⁻¹; Yu and McPhaden, 1999).
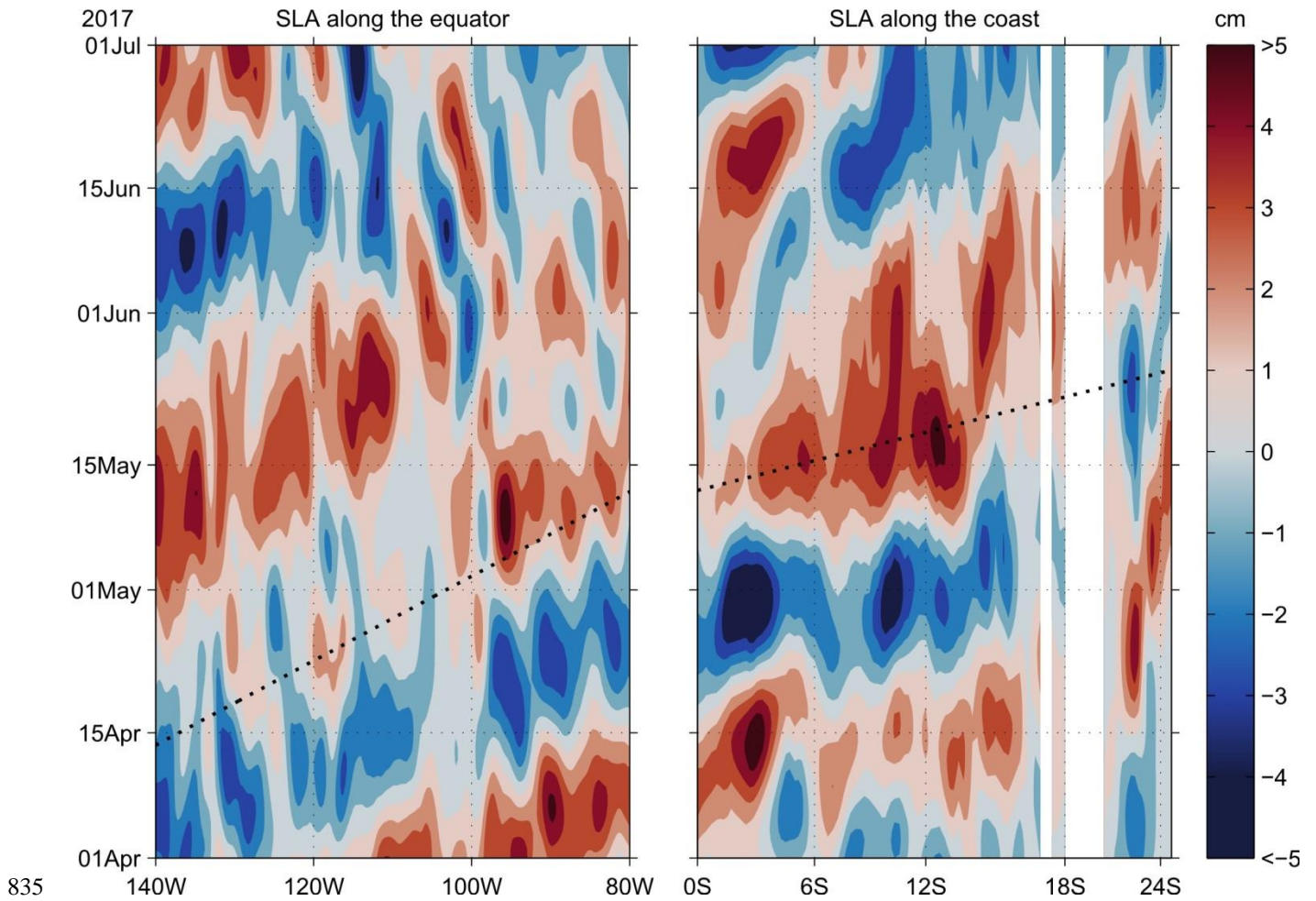
Figure 7: Bandpass filtered (20 – 90 days) sea level anomaly along the eastern equatorial Pacific averaged between 0.25°N and 0.25°S (left panel) and along the western coast of South America (right panel) averaged over the two grid point closest to the coastline. The propagation of a first mode equatorial Kelvin wave and CTW are shown as dotted black lines, phase speed of the equatorial wave is 2.7 m s⁻¹ (Yu and McPhaden, 1999) and 3.1 m s⁻¹ for CTWs (see figure 8b).

835

840
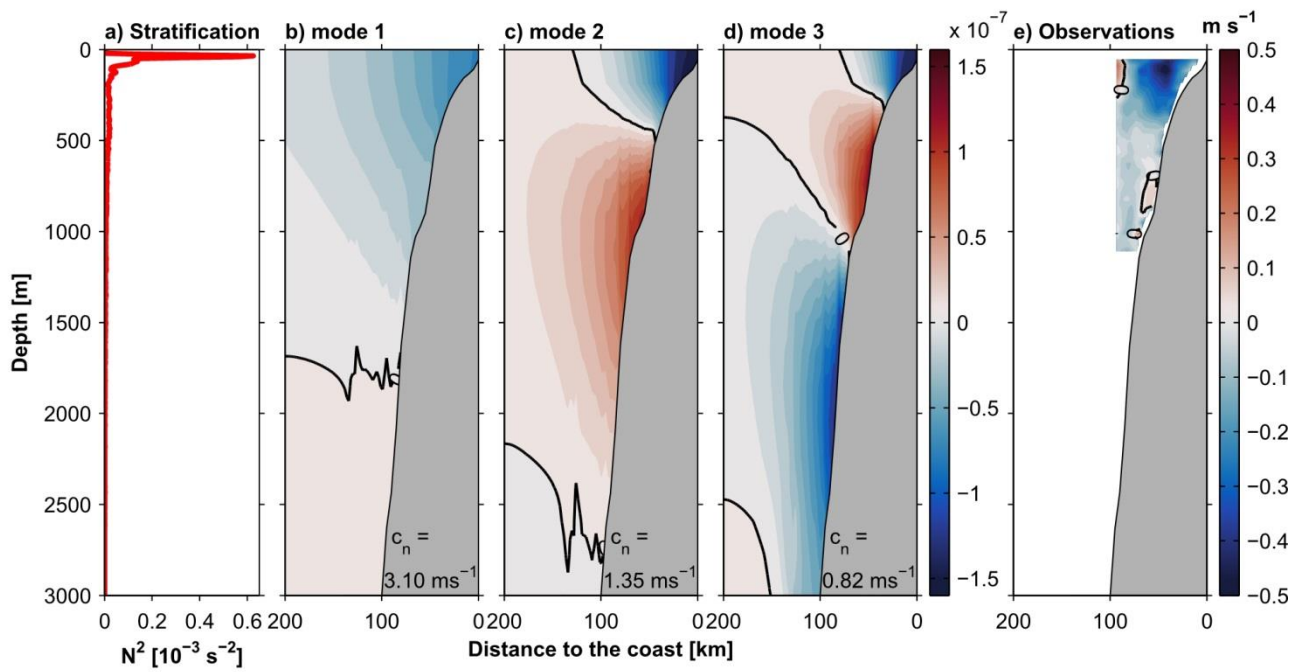
Figure 8: Profile of stratification (N^2) (left panel) and cross-shore-depth structure of alongshore velocity (arbitrary amplitude) obtained for the first three CTW modes (panel b through d). Panel e) shows the difference of observed alongshore velocity between April 18 – May 03 and May 12 – 26, 2017. Note that the CTW phase speeds c_n are given in the lower right corner of the respective velocity structure panel.
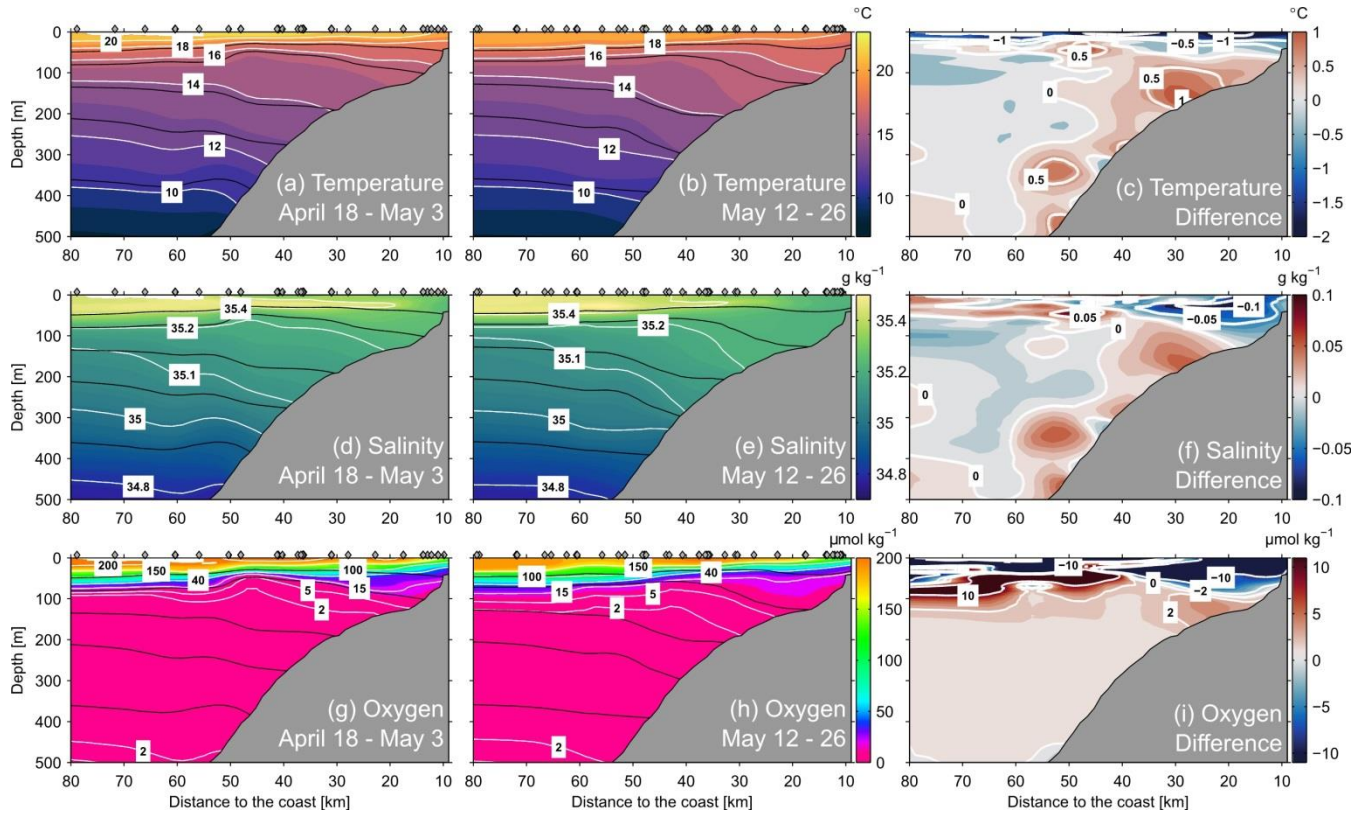
Figure 9: Conservative temperature (upper panel row), absolute salinity (middle panel row), and oxygen (lower panel row) at 12° S during April 18 – May 3, 2017 (left panel column) and May 12 – 26, 2017 (middle panel column). The difference of the respective characteristic between the two periods is indicated in the right panels. Black lines indicate the distribution of isopycnals (σ$_\theta$) 25.6, 25.9, 26.2, 26.4, and 26.7 kg m^{-3}. Grey diamonds mark positions of CTD stations.

855
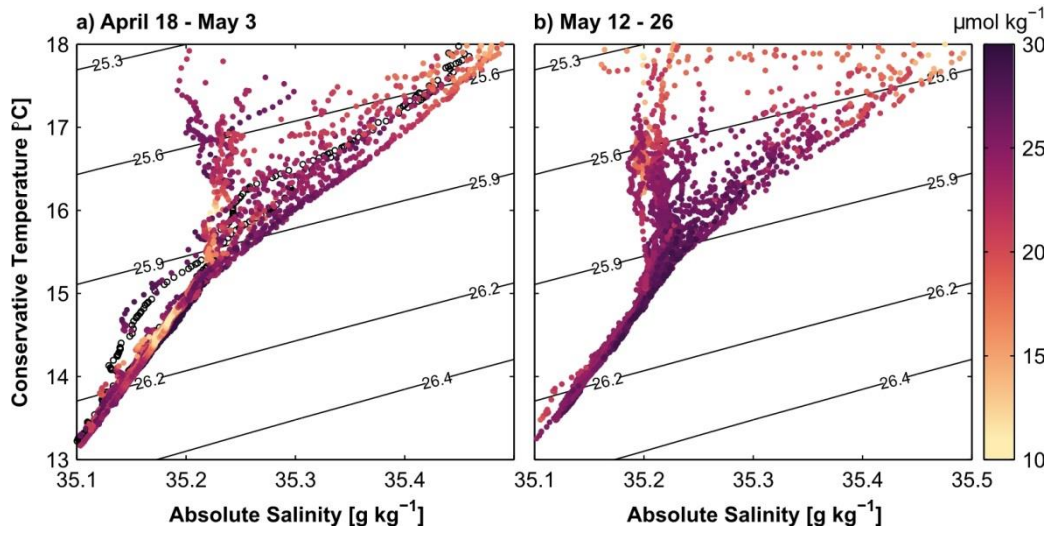
860 **Figure 10: Conservative temperature – absolute salinity diagram between 50 and 300 m depth for CTD profiles between the 100 and 400 m isobaths during April 18 – May 3, 2017 (left panel) and May 12 – 26, 2017 (right panel). Colour code depicts nitrate concentrations. Black contours indicate isopycnals (σ_θ) in kg m^{-3}.**
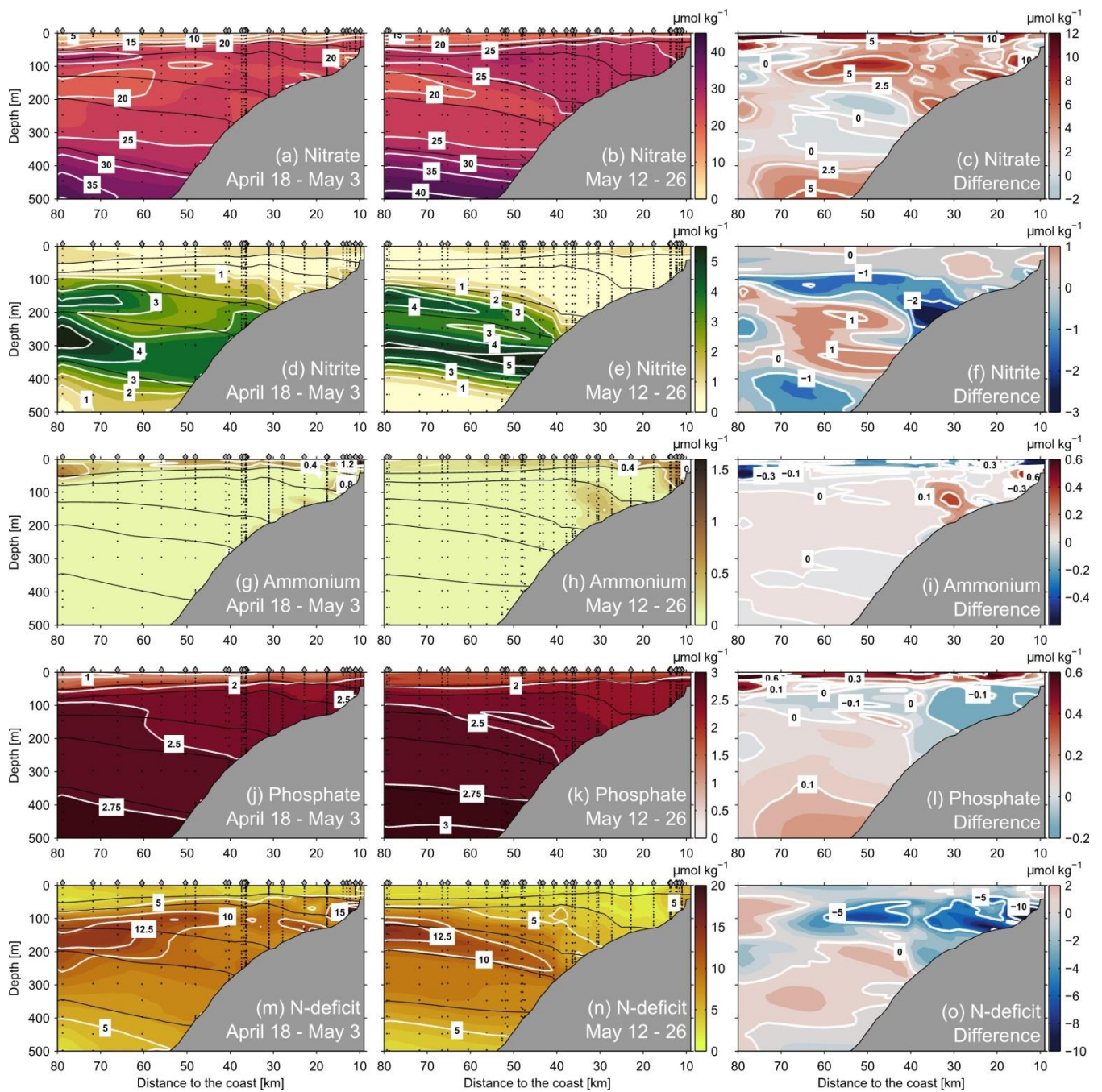
Figure 11: Nitrate (upper panels), nitrite (2ⁿᵈ panel row), ammonium (3ʳᵈ panel row), phosphate (4ᵗʰ panel row) concentrations, and nitrogen deficit (bottom panel row) at 12° S during April 18 – May 3, 2017 (left panels) and May 12 – May 26, 2017 (middle panels). Concentration difference of the respective parameters between the two time periods are shown in the left panels. Black lines indicate the distribution of isopycnals (σ_θ) the 25.6, 25.9, 26.2, 26.4, and 26.7 kg m⁻³. Grey diamonds mark the positions of CTD stations while black circles mark the position of bottle samples in the water column.
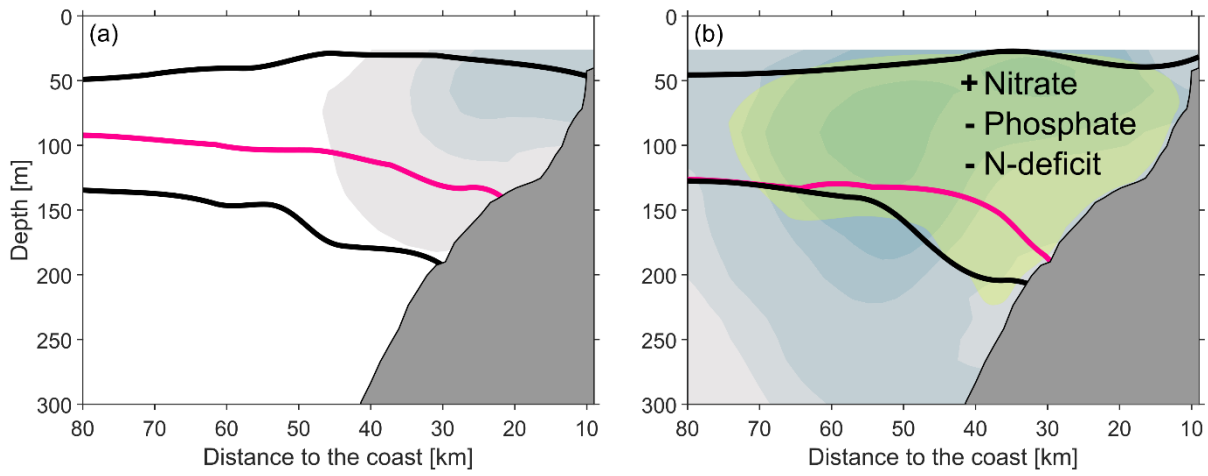
870

Figure 12: Schematic of the conditions off Peru during the initial phase of weak PCUC flow (a) and strong PCUC flow (b). Alongshore circulation is shown as colour shading, two isopycnals are sown in black and the top of the anoxic zone in magenta (represented by the 2 µmol kg^{-1} isoline). The green shaded area in (b) shows the region of increased nitrate, decreased phosphate concentrations and decreased nitrogen deficit.